Macro-permeability distribution and anisotropy in a 3D fissured and fractured clay rock: 'Excavation Damaged Zone' around a cylindrical drift in Callovo-Oxfordian Argilite (Bure)

Rachid Ababou [a,*], Israel Cañamón Valera [b], Adrien Poutrel [c]

[a] IMFT, Institut de Mécanique des Fluides de Toulouse, 1 Allée Camille Soula, 31400 Toulouse, France
[b] UPM, Universidad Politécnica de Madrid, E.T.S.I. Minas, Dep. de Matemática Aplicada y Métodos Informáticos, C./Ríos Rosas 21, 28003 Madrid, Spain
[c] ANDRA, Agence Nationale pour la Gestion des Déchets Radioactifs, 1/7 rue Jean Monnet, Parc de la Croix-Blanche, 92298 Châtenay-Malabry Cedex, France

Keywords:
Equivalent permeability tensor
Gallery and EDZ
Fractured clay rock
Matrix/Fracture superposition
Anisotropy
Radioactive waste disposal

A B S T R A C T

The Underground Research Laboratory at Bure (CMHM), operated by ANDRA, the French National Radioactive Waste Management Agency, was developed for studying the disposal of radioactive waste in a deep clayey geologic repository. It comprises a network of underground galleries in a 130 m thick layer of Callovo-Oxfordian clay rock (depths 400–600 m). This work focuses on hydraulic homogenization (permeability upscaling) of the Excavation Damaged Zone (EDZ) around a cylindrical drift, taking into account: (1) the permeability of the intact porous rock matrix; (2) the geometric structure of micro-fissures and small fractures synthesized as a statistical set of planar discs; (3) the curved shapes of large 'chevron' fractures induced by excavation (periodically distributed).

The method used for hydraulic homogenization (upscaling) of the 3D porous and fractured rock is based on a 'frozen gradient' superposition of individual fluxes pertaining to each fracture/matrix block, or 'unit block'. Each unit block comprises a prismatic block of permeable matrix (intact rock) obeying Darcy's law, crossed by a single piece of planar fracture obeying either Darcy or Poiseuille law. Polygonal as well as disc shaped fractures are accommodated. The result of upscaling is a tensorial Darcy law, with macro-permeability $K_{ij}(\mathbf{x})$ distributed over a grid of upscaling sub-domains, or 'voxels'. Alternatively, $K_{ij}(\mathbf{x})$ can be calculated point-wise using a moving window, e.g., for obtaining permeability profiles along 'numerical' boreholes. Because the permeable matrix is taken into account, the upscaling procedure can be implemented sequentially, as we do here: first, we embed the statistical fissures in the matrix, and secondly, we embed the large curved chevron fractures.

The results of hydraulic upscaling are expressed first in terms of 'equivalent' macro-permeability tensors, $K_{ij}(x, y, z)$ distributed around the drift. The statistically isotropic fissures are considered, first, without chevron fractures. There are 10,000 randomly isotropic fissures distributed over a 20 m stretch of drift. The resulting spatially distributed K_{ij} tensor is nearly isotropic (as expected). At the scale of the whole EDZ, the global K_{FISSURES} is roughly 5000 times larger than permeability K_M. The detailed distribution of the equivalent $K_{\mathrm{FISSURES}}(x, y, z)$ defined on a grid of voxels is radially inhomogeneous, like the statistics of the disc fissures. In addition, a moving window procedure is used to compute detailed radial profiles of K_{FISSURES} versus distance (r) to drift wall, and the results compare favorably with *in situ* permeability profiles (numerical *vs.* experimental boreholes at Bure's GMR drift).

Finally, including the large curved chevron fractures in addition to the random fissures, the resulting $K_{ij}(x, y, z)$ appears strongly anisotropic locally. Its principal directions are spatially variable, and they tend to be aligned with the tangent planes of the chevron fracture surfaces. The global equivalent K_{ij} of the whole EDZ is also obtained: it is only weakly anisotropic, much less so than the local K_{ij}'s. However, because of the radially divergent structure of the 'chevrons' (although not quite cylindrical in geometry), it is recognized that the global K_{ij} due to chevrons lacks physical meaning as a tensor. Considering only the magnitude, it is found that the permeability due to 'chevrons' (K_{CHEVRONS}) is about 4 orders of magnitude larger than that due to statistical fissures (K_{FISSURES}), assuming a hydraulic aperture $a_{\mathrm{CHEVRON}} = 100\ \mu\mathrm{m}$. By a simple argument, K_{CHEVRONS} would be only one order of magnitude larger than K_{FISSURES} with the choice $a_{\mathrm{CHEVRON}} = 10\ \mu\mathrm{m}$ instead of 100 μm. This significant sensitivity is due to several

* Corresponding author.
E-mail addresses: ababou@imft.fr (R. Ababou), israel.canamon@upm.es (I. Cañamón), adrien.poutrel@andra.fr (A. Poutrel).

factors: the large extent of chevron fractures, the assumption of constant hydraulic aperture, and the cubic law behavior based on the assumption of Poiseuille flow.

The equivalent macro-permeabilities obtained in this work can be used for large scale flow modeling using any simulation code that accommodates Darcy's law with a full, spatially variable permeability tensor $K_{ij}(\mathbf{x})$.

1. Introduction

The Underground Research Laboratory at Bure (CMHM – Centre de Meuse/Haute Marne, France) is operated by ANDRA, the French National Radioactive Waste Management Agency. The purpose of the laboratory is to study the disposal of radioactive waste in a deep clayey geologic repository. The laboratory comprises a network of underground galleries through a 130 m layer of Callovo-Oxfordian "argilite", or clay rock, about 155 million years old, and located between 400 m and 600 m depth.

In this context, the present work focuses on the hydraulic homogenization (upscaling) of the Excavation Damaged Zone (EDZ) around a cylindrical excavation (gallery), taking into account the specific geometric structure of two sets of dicontinuities: (i) the 'fissures' comprising in fact microfissures as well as minor fractures (submetric) and (ii) the much larger curved shear fractures organized in a 'chevrons' pattern. The latter are induced by (ahead of) the excavation front, and have an extension of several meters. In addition, the permeability of the intact porous rock is also directly taken into account.

In summary, the 'damaged' heterogeneous medium is made up of three sets of conductors: (i) microfissures and moderate size fractures (submetric); (ii) large curved 'chevron' fractures (several meters); and (iii) intact porous matrix (undisturbed clay rock).

Two different geometric models are used for structuring the two sets of discontinuities in 3D space: (i) the 'fissures' are represented as a *statistically isotropic set of planar discs*; and (i) the 'chevron' fractures are represented as a *periodic set of curved parametric surfaces*.

The results of hydraulic upscaling (to be explained further below) are expressed mainly in terms of 'equivalent' *macro-permeability tensors*. The macro-permeabilities obtained in this work will be compared against *in situ* data, namely, permeability profiles along boreholes.

2. Geometric and statistical modeling of the 'EDZ' in 3D

In this paper, we consider a 3D stretch of a cylindrical excavation (gallery or drift), with the following geometry: (i) section length $L = 20$ m; (ii) drift diameter $D_{\mathrm{DRIFT}} = 4$ m; (iii) thickness of the annular EDZ around the drift: $E = 4$ m. The chosen domain of investigation is a 3D rectangular box of size 20 m $\times$ 13 m $\times$ 13 m, which encloses the drift and its 'EDZ'.

The transverse scales for the drift and EDZ correspond roughly to the experimental drifts excavated at Bure and the observed EDZ. For convenience, the drift length was shortened from about 100 m to 'only' 20 m. This does not affect the 3D hydraulic upscaling study conducted in this paper, given the statistical homogeneity of the EDZ along the drift axis.

The goal of this section is to present a geometrical and statistical model of the 3D structure of the clay rock in the Excavation Damaged Zone (EDZ), on which the rest of the paper is based.

2.1. Statistical network of fissures (random plane discs)

The 'fissures' (microfissures and small fractures) are modeled as statistical set of planar discs, with randomly isotropic orientations, and radially decreasing density, diameters and apertures away from the drift wall : a visualization is shown in Fig. 1.

The main hypotheses for the statistical set of discrete fissures were:

- The fissures are plane discs with statistically isotropic orientations in 3D euclidian space.
- Their planar size is a random variable (random radius R or random diameter D).
- Their thickness or 'aperture' is a random variable (random aperture 'a').
- Their euclidian positions (X, Y, Z) are random: they follow a modified Poisson-type process such that the volumetric density of fissures (ρ_{03}) is radially inhomogeneous (decreasing)...

The volumetric density $\rho_{03}(r)$ expresses the number of discrete 'objects' per m^3 of euclidian space, as explained in Appendix A. This appendix provides a "*geometric probability*" analysis of radial inhomogeneity, and particularly, of the relation between volumetric density $\rho_{03}(r)$ and the Probability Density Function (PDF) of fissure centers positions (X, Y, Z).

Given our choices, as will be seen, $\rho_{03}(r)$ decreases quite fast with radial distance 'r' from the drift wall, and so does the mean fissure radius R and the mean aperture 'a'. These are maximal at the drift wall. For example:

- the maximum aperture of fissures (at the drift wall) is: $a_{\mathrm{MAX}} = 5.0\,\mathrm{E}-5$ m (50 μm);

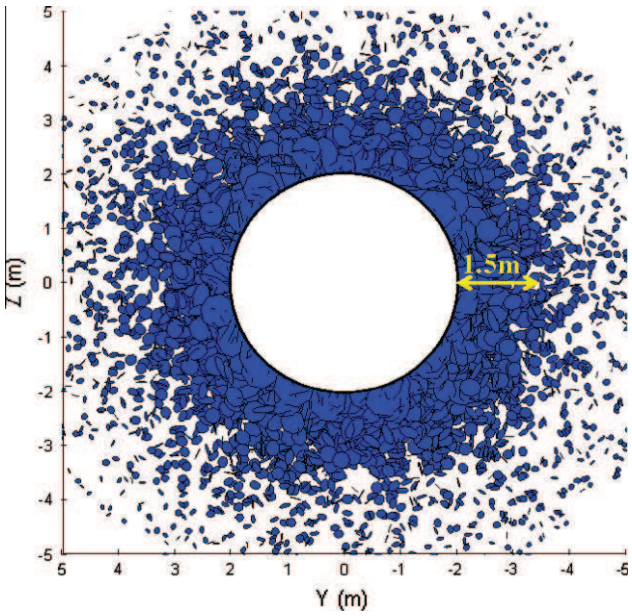

Fig. 1. Front view of the set of 10,000 planar disc fissures on the transverse vertical plane at the drift entrance (3D view with hidden parts). As can be seen, density and diameters decrease radially (so do the apertures, although they are not visible in this view).

- the maximum size of fissures (at the drift wall) is: R_{MAX} = 0.40 m (diameter 80 cm).

On the other hand, for simplicity, fissures orientations are assumed isotropic at any distance '*r*' from the drift wall: in other words, orientations are isotropic and statistically homogeneous in space. Appendix B (Tables B.1–B.3) provide details on the chosen statistical distributions of fissure parameters, and in particular, their inhomogeneous radial distribution.

Finally, it should be emphasized that the selected parameters are not arbitrary. They were determined by trial and error. They lead to a fairly good fit between theoretical (upscaled) and actual (measured) permeabilities $K(r)$ along radial boreholes at the Bure URL site (Section 5).

2.2. Deterministic set of curved fractures ('chevrons')

The extensive shear fractures observed in the EDZ at Bure are distributed more or less periodically according to a 3D '*herringbone*' or '*chevron*' pattern (for convenience, the fractures themselves will be named '*chevrons fractures*'). Accordingly, we have chosen to represent the chevron fractures deterministically, as a set of surfaces periodically distributed along the axis of the gallery. Furthermore, it was decided that each individual fracture should be represented mathematically by a curved parametric surface, analogous as much as possible to the fracture shapes observed in the Bure drifts. Indeed, the observed 'chevrons fractures' at the Bure URL appear to have fairly complex curved shapes in 3D (Armand, 2007).

With this in mind, our primary objective was to take into account the geometric complexity as much as possible, via a *parametric surface* possessing most of the curvatures and cusps observed in the actual galleries at Bure. This was investigated for a typical case (the GMR drfit at Bure) without necessarily trying to address all the effects of particular conditions, such as the direction of the drift (parallel to major or minor horizontal principal stress), or the location within the drift (near or far from the excavation front), etc.

The parametric surface model retained here is a "*generalized elliptic conoïd*", developed by us as an extension of other known conoïdal surfaces, such as the elliptic conoïd of Isawi (*it.wikipedia.org/wiki/Conoide_ellittico*). The latter is itself derived from the classical conoïdal surface of Wallis, known for centuries. Wallis' conoïd is also known as "*conical wedge*", "*conocuneus*", and "*arrière-voussure de Saint-Antoine*" in architecture. It has the same shape as the pinched end of a toothpaste tube. Several other types of conoïds were explored: for instance, Plücker's conoïd of order 2 has the shape of a pancake pinched at its center (not quite suitable for our purpose). Another interesting surface which came close (but not quite) to the shape of a chevron fracture was the Guimard surface, which can be observed as the glass roof located at the entrance of the "Abbesses" metro station near Montmartre in Paris.

Finally, as a result of these investigations, our 'best' model so far is the "*generalized elliptic conoïd*". It has the following parametric equation:

$$\vec{S}=\begin{pmatrix}x\\y\\z\end{pmatrix}=\begin{pmatrix}(a\cdot(1-u)+c\cdot u)\cdot\cos(v)\\(d\cdot u^{(d1\cdot(1-EX)+d2\cdot EX)})\cdot\sin(v)\\b\cdot(1-u^2)\cdot|\cos(v)|^g+e\cdot u^{(e1\cdot(1-EX)+e2\cdot EX)}+f\cdot u^{(f1\cdot(1-EX)+f2\cdot EX)}\end{pmatrix}$$
$$\text{with: } v\in[0,2\pi];\ u\in[0,1]$$
$$\text{and: } EX(v,n)=\left[1-\left|(\cos(v))^{|\tan(n\cdot\pi+\pi/2)+1|}\right|\right]\cdot(1-n)+\left|(\sin(v))^{|\tan(n\cdot\pi+\pi/2)+1|}\right|\cdot n, \quad (1)$$

where '*n*' is a real number between 0 and 1 (we selected here the value $n = 0.1$). The parameters finally selected to represent typical chevron fractures at the Bure site are:

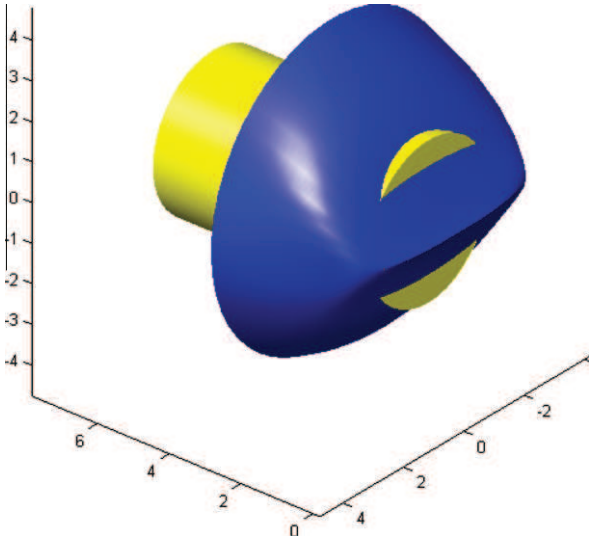

Fig. 2. 3D view of a 'chevron' fracture surface obtained with a complex elliptic 'conoïd'. Note: synthetic traces were compared with observed traces (Bure/GMR drift).

$a = 2.75$, $b = 0.4$, $c = 4$, $d = 4$, $e = 1.5$, $f = 2$, $g = 3$,
$d1 = 0.5$, $d2 = 1.75$, $e1 = 2$, $e2 = 8$, $f1 = 1.25$, $f2 = 1.5$, $n = 0.1$

In particular, these parameter values 'optimize' the representation of chevron fractures in Bure's GMR gallery, which is oriented parallel to the minor horizontal principal stress (σ_h).

Fig. 2 shows a 3D perspective view of the chosen mathematical surface, representing a single 'chevron' fracture positioned around a cylindrical gallery.

Fig. 3 below shows a comparison between:

- The conoïdal mathematical surface (defined above), and
- In situ observations (fracture traces in the GMZ gallery at Bure).

It can be seen from Fig. 3 that the selected mathematical surface (generalized elliptic conoïd), resembles the curved shapes of actual chevron fractures based on observed traces projected on vertical and horizontal planes.

Finally, by superimposing the clay rock matrix + planar disc fissures + chevron fractures, we obtain the complete structure of the EDZ, as show for instance in Figs. 4a and 4b. Note: the intact clay rock matrix is *not visible* in any of these 3D views – only the discrete fissures and fractures are visualized. Nevertheless, matrix porosity and matrix permeability are fully taken into account in the hydraulic upscaling procedure (matrix permeability is not neglected).

3. Hydraulic upscaling and macro-permeability tensor for a fissured/fractured porous medium (superposition method)

We present in this section the method adopted for homogenizing or 'upscaling' flow in the 3D disturbed clay rock of the EDZ, comprising a porous matrix (intact clay), a set fissures (planar disc shaped microfissures and small fractures), and a set of fractures (large nonplanar "chevron" fractures).

3.1. Introduction and overview on upscaling by superposition

3.1.1. Overview on the superposition method

Briefly, the hydraulic upscaling method used here consists in superposing local fluxes based on a "frozen gradient"

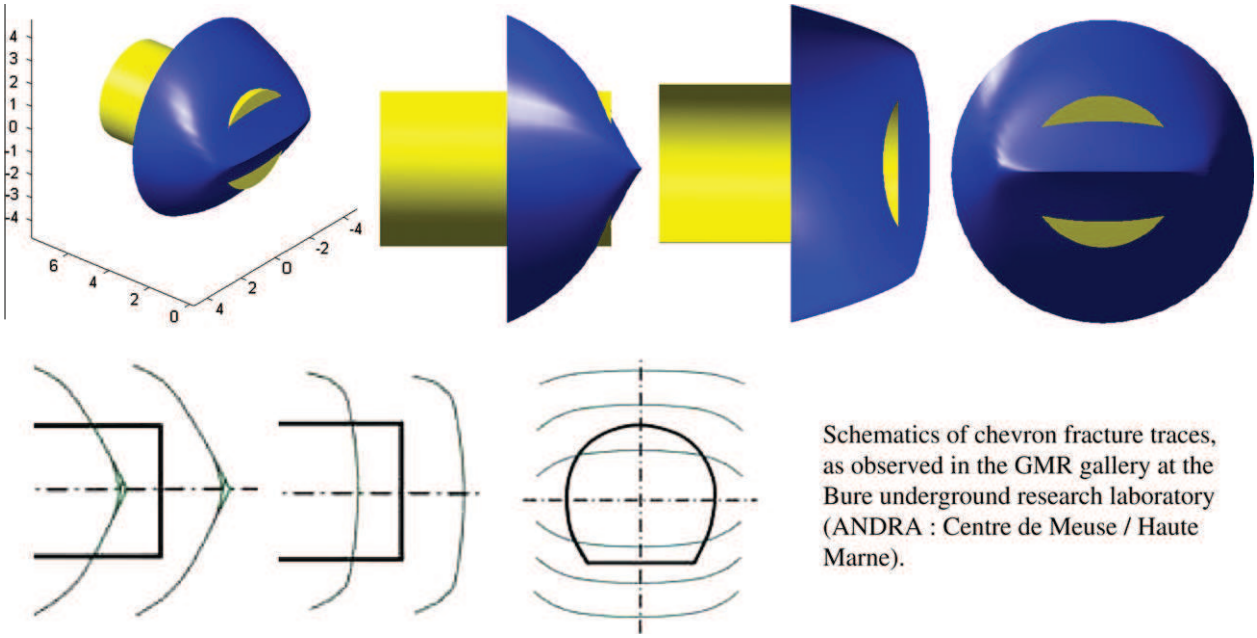

Fig. 3. Morphology of the curved surfaces of large shear fractures ('chevrons'). Above. Various 3D perspective views of the «generalized elliptic conoïd», the approximate surface model retained for describing the curved surfaces of 'chevrons' fractures at the Bure clay rock site (ANDRA's URL: Centre de Meuse/Haute Marne). Below. Comparison with the traces of chevron fractures observed at Bure in the GMR gallery (aligned with the minor horizontal principal stress σ_h): the schematic show the traces projected on the axial vertical plane, axial horizontal plane, and transverse plane, respectively. [Internal reference: ANDRA-Synthèse Geoter (2007, Appendix C) and ANDRA Document 'DRP0GTR060003'].

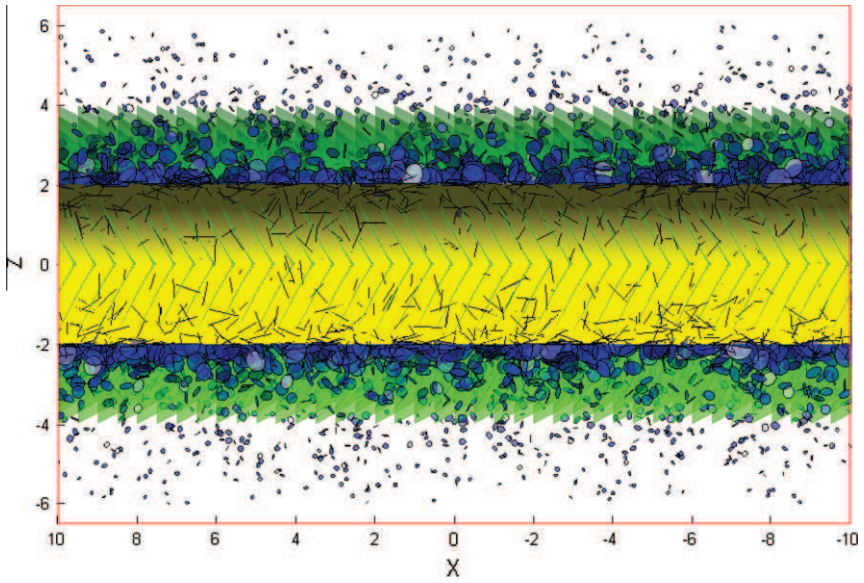

Fig. 4a. A 3D front view of the synthetic drift (20 m stretch) with its surrounding clay rock (EDZ), showing (i) the statistical set of plane disc fissures and (ii) the periodic set of large curved fractures ('chevron' pattern). Only one half of the drift is shown, 'behind' the central axial vertical plane. All chevron fractures can be seen (they are slightly translucent). Many of the random discs are hidden by the drift. Traces of both chevron and disc fissures are visible on the cylindrical drift surface.

approximation. It will thus be named here "flux superposition approach" and/or "frozen gradient approach". This superposition approach is not exact as a whole, except in some special cases. In general, it tends to overestimate the permeability tensor K_{ij} (Appendix C discusses this point and briefly analyzes the theoretical nature, properties and range of validity of the approach).

In the case of a fracture network, this method obtains the equivalent permeability by summing the fluxes of all fractures, assuming each fracture flux to be produced by the same constant (frozen) mean pressure gradient. The result is a tensorial anisotropic version of Darcy's law with macro-permeability K_{ij}. This approach was initially proposed by Snow (1969) and Kiraly (1969) for various hydrogeologic situations, and was later developed by Oda (1986) and Ababou (1991). The latter author presents an extensive review on fracture flow, and develops the equivalent permeability tensor K_{ij} (superposition approach) for discrete networks comprising several statistical sets of fractures. In addition, a similar approach was developed for coupled Thermo-Hydro-Mechanics in elastic fractured rocks (Oda (1986), Ababou et al. (1994b), Stietel et al. (1996)).

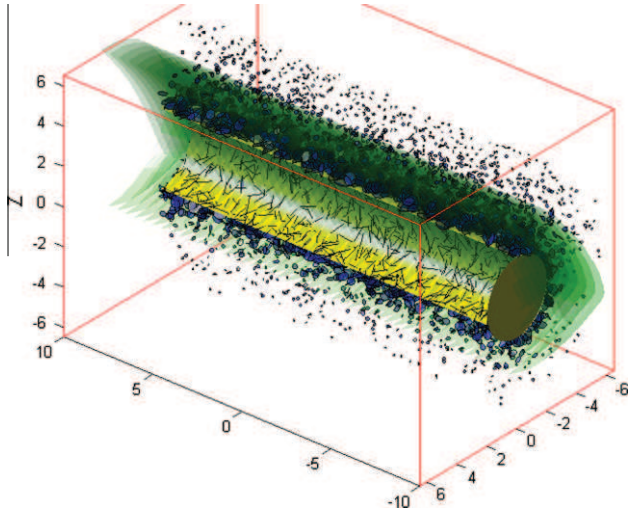

Fig. 4b. A 3D perspective view of the synthetic drift (20 m stretch) with its surrounding clay rock (EDZ), showing the statistical set of plane disc fissures and the periodic set of large curved 'chevron' fractures.

However, in all the above-quoted works, the permeability of the porous matrix between fractures was neglected (which is *not* our assumption here). The advantage of taking into account *matrix permeability* is manyfold. *First*, it opens up the possibility of studying the case of a fractured medium with a micro-damaged porous matrix without having to represent explicitly the damaged microstructure. *Secondly*, it allows us to implement more flexible variants such as iterative or sequential upscaling: specifically here, the statistically isotropic fissures are upscaled first, and only then, the large curved chevron fractures.

The extension of the superposition approach to the case of nonnegligible rock matrix permeability is not trivial. Indeed, accounting for rock matrix permeability renders the upscaling more complex because it is now necessary, in the superposition approach, to sum over prismatic "unit blocks" (rather than planar fractures). Furthermore, one must first define, for each unit block, the effective influence of the permeability of the matrix surrounding each piece of plane fracture.

The extension to permeable fractured media was first presented in Cañamón (2006) and Cañamón et al. (2007). In fact, the method implemented in the sequel of this paper is itself an extension of these works. It involves the following features (items (c)–(e) are new):

(a) The geometry of the medium is fully 3D.
(b) The case of a porous rock matrix with nonzero permeability is treated (rather than the case of a 'pure' discrete conductor network, as explained above).
(c) The set of statistical 'conductors', the planar disc fissures, is statistically inhomogeneous in 3D space (it is inhomogeneous along radial directions from the central axis of the drift).
(d) The discrete 'conductors' include not only the statistical set of planar fissures, but also, another set of large nonplanar features (chevron fractures modeled as curved surfaces).
(e) The 3D hydraulic conductivity is upscaled on various types of 'supports', such as: local cubic voxels distributed in 3D space around the drift; elongated windows distributed in 2D transverse space; and mobile spherical windows along radial directions (numerical boreholes).

Finally, concerning upscaling methods other than superposition, see Renard (1997), Renard and de Marsily (1997), Bailly et al. (2009), and references therein. Interestingly, our matrix/fracture superposition method has connections with the so-called *self-consistent* method, whose first step is basically a superposition. However, the rest of the *self-consistent* procedure is different. The important feature of the superposition method in the present work is that it involves nothing else than a weighted sum of matrix/fracture properties, which can be implemented in two possible ways:

- as a probabilistic integral or a mathematical expectation over ensemble space (Oda, 1986);
- as a discrete and deterministic sum of distributed properties over 3D space (*as we do here*).

3.1.2. Overview on upscaling coefficients (macro-permeability K_{ij})

Let us now briefly describe the type of results to be obtained by the superposition approach (to be presented in the next sections of this paper).

The flux superposition method is a "linearized" method for upscaling Darcy/Poiseuille type flow. Therefore, it leads to a linear Darcy-type macroscale law relating the macroscale flux to the macroscale hydraulic gradient, via a tensorial anisotropic macro-permeability K_{ij}. The macro-permeability can be calculated explicitly at any point in space (x, y, z) or for any upscaling block (i, j, k), without need for numerical flow simulations. There is much flexibility concerning the scale, size and dimensionality of the upscaling blocks.

In summary, the result obtained is an upscaled equivalent Darcy law, with tensorial macro-permeability $K_{ij}(\underline{\boldsymbol{x}}_{IJK})$ defined on a grid of upscaling blocks or 'voxels' ($\underline{\boldsymbol{x}}_{IJK}$). Alternatively, the tensor $K_{ij}(\underline{\boldsymbol{x}})$ can also be produced "pointwise" in continuous space ($\underline{\boldsymbol{x}}$) using a moving window for upscaling. Indeed, this procedure will be used in this work to obtain "numerical" borehole profiles $\boldsymbol{K}(\boldsymbol{r})$ radially with respect to the center of the gallery.

In all cases, the macroscale K_{ij} tensor contains relevant information about the local properties of the rock, such as the friction parameters (matrix permeability) and the geometry and density of the discrete set of conductors (apertures, density, specific areas). Of course, K_{ij} may also depend (mildly) on the shape of the upscaling window used: cubic, spherical, etc.

The specific implementation of the upscaling method for the 3D fissured/fractured 'EDZ' is now explained in more detail below.

3.2. Implementation steps of hydraulic upscaling for the case of the fissured/fractured 'EDZ' around a cylindrical drift

3.2.1. First step: equivalent permeability of unit blocks (upscaling single fracture/matrix blocks)

The hydraulic upscaling method is implemented for a fully 3D matrix/fracture composite, based on a 'frozen gradient' superposition of 'local' flux vectors. But these local flux vectors must first be computed for each single fracture/matrix block, or "unit block". The aim of this sub-section is to propose an "exact" equivalent permeability tensor for each unit block (the term "exact will be discussed at the end of this sub-section).

A 'unit block' comprises a single piece of plane fracture obeying either Darcy or Poiseuille law, surrounded by a permeable porous matrix (the intact rock) governed by Darcy's law. Planar disc fractures as well as polygonal fractures imbedded in a permeable porous matrix can be accommodated, all this in 3D space.

Specifically, a "unit block" is formed by a polygonal piece of fracture (with straight or curved edges) plus 2 polygonal prismatic volumes of matrix on either side of it ('upper' and 'lower' half-matrix blocks). These two prismatic volumes have the same thickness $b/2$, and the total thickness of the block is therefore "b" (neglecting fracture aperture "a", but only here, just for simplicity). The thicknesses "b" of the different blocks located in a given upscaling sub-domain are the same. A unique choice of parameter

"b" preserves the total volume and volume fractions of fractures and matrix. These conservation principles lead to:

$$b = 2 \Big/ \sum_m \sigma_m,$$

where σ_m is the specific area of fracture "m" within the sub-domain at hand.

See Cañamón (2006) and Cañamón et al. (2007) for more details. This matrix/fracture procedure generalizes previous approaches developed for the special case of impervious matrix by Oda (1986); Ababou (1991); Ababou et al. (1994a,b).

Now, the first step of the method is to calculate *exactly* the equivalent permeability of each "unit block", i.e., each piece of fracture with its surrounding matrix. This first step is done under conditions of piecewise constant hydraulic gradient condition on the boundaries of the unit block, such that the resulting equivalent permeability tensor is obtained exactly analytically (as explained in Cañamón (2006) and Cañamón et al. (2007)).

Fig. 5 depicts a simplified parallelepipedic version of the unit block, in the local frame of the fracture plane. The thickness of the surrounding matrix is calculated based on statistical densities (mean spacing or inverse specific area). More general prismatic blocks can be accommodated as well. Note: block shapes depend on the geometry of fractures (polygons, discs) but also on the geometry of upscaling windows (cubic voxels, spherical windows...).

The local permeabilities inside each medium (fracture, matrix) are tensorial quantities defined as follows in the local reference frame (e_1, e_2, e_3) of the unit matrix/fracture block:

$$(K_M^*) = \begin{pmatrix} K_M & 0 & 0 \\ 0 & K_M & 0 \\ 0 & 0 & K_M \end{pmatrix}_{(e_1,e_2,e_3)} \qquad (K_F^*) = \begin{pmatrix} K_F^{ll} & 0 & 0 \\ 0 & K_F^{ll} & 0 \\ 0 & 0 & K_F^{\perp} \end{pmatrix}_{(e_1,e_2,e_3)} \tag{2}$$

where K_M is matrix permeability (Darcy), K_F^{ll} is "fracture permeability" parallel to the fracture plane (either Darcy or Poiseuille), and $K_F^{\perp}$ is "fracture permeability" perpendicular to fracture plane ($K_F^{\perp} = K_F^{ll}$ for a Darcy fracture, $K_F^{\perp} = \infty$ for a Poiseuille fracture). Without going into details, the final result for the exact equivalent permeability of the unit block Ω_1 is:

$$\left(\overline{K_{MF}^*}\right)_{\Omega_1} = \begin{pmatrix} K_A & 0 & 0 \\ 0 & K_A & 0 \\ 0 & 0 & K_H \end{pmatrix}_{(e_1,e_2,e_3)} \quad \text{with :} \quad \begin{aligned} K_A &= (1-\phi_F)K_M + \phi_F K_F^{ll} \\ K_H &= \left(\tfrac{1-\phi_F}{K_M} + \tfrac{\phi_F}{K_F^{\perp}}\right)^{-1} \end{aligned} \tag{3}$$

where ϕ_F is the volumetric fraction of the single fracture (per volume of the 'unit block').

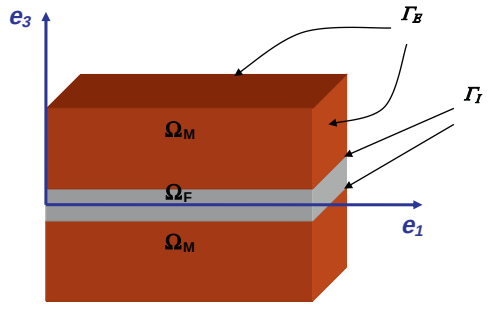

Fig. 5. Schematic of a 'unit block' Ω_1. A unit block is a single fracture/matrix block made up of a piece of fracture plane Ω_F surrounded on each side by the porous matrix Ω_M.

Finally, using the unit vector ($\mathbf{n}$) normal to the fracture plane, we can express the equivalent permeability tensor of each matrix/fracture unit block, in the global reference frame:

$$\left(\overline{K_{MF}^{ij}}\right)_{\Omega_1} = (\delta_{ij} - n_i n_j)\cdot K_A + n_i n_j K_H \tag{4a}$$

and the equivalent Darcy law at the scale of a unit block Ω_1 can be expressed as:

$$(q_i)_{\Omega_1} = \left(\overline{K_{MF}^{ij}}\right)_{\Omega_1} (J_j)_{\Omega_1} \quad \text{(Einstein's implicit summation on repeated indices)} \tag{4b}$$

where $\mathbf{q}_{\Omega 1}$ is the flux density vector (m/s) and $\mathbf{J}_{\Omega 1}$ the hydraulic gradient (−gradH).

In closing, we consider briefly two issues: what about the case of non-isotropic matrix permeability? and in what sense is the result obtained above an exact equivalent K_{ij}?

- The permeable matrix "M" was assumed isotropic in the above equations. Although it is possible to extend the exact unit block upscaling (Eq. (4)) to the case of anisotropic matrix, we will not do so here, for reasons explained later in the application section (cf. Section 4.1).
- For a given heterogeneous block, without any other specification, there is no unique equivalent permeability tensor, as observed by Pouya and Fouché (2009). But we are being more specific here. The above results (Eqs. (2)-(4)) demonstrate that there a unique equivalent permeability tensor K_{ij} for the unit fracture/matrix block, under a particular type of boundary conditions (piecewise linear hydraulic heads along the boundary of the sample). Moreover, the same tensor K_{ij} can also be obtained equivalently under piecewise constant flux boundary conditions.

3.2.2. Second step: flux superposition (frozen gradient approximation)

As explained earlier, we now apply the flux superposition approach to the set of all 'unit blocks', assuming a "frozen" macroscale gradient (the macroscale is the scale of the upscaling domain, cubic voxel or spherical window). While the unit block upscaling done in the first step was in a sense "exact", the flux superposition method implemented in this second step is only approximate, and it usually leads to an overestimation of the final permeability tensor K_{ij}, as explained in Appendix C.

The equivalent permeability K_{ij} of the domain Ω is obtained by summing the individual fluxes of all unit blocks (the single fracture/matrix blocks), using the previously obtained equivalent block permeability tensor, and applying the same fixed mean pressure gradient to all unit blocks (constant frozen gradient approximation). The total flux vector (m^3/s) is obtained by volumetric summation over the whole upscaling domain Ω as follows:

$$(\overline{Q})_\Omega = \sum_k (\overline{Q})_\Omega^k \text{ with } (\overline{Q})_\Omega^k = \frac{\int_{\Gamma_E} (\bar{q})_\Omega^k ds}{2} = A_{OUT}^k \cdot (\bar{q})_\Omega^k \tag{5}$$

where $(\overline{Q})_\Omega^k$ is the flux vector associated with fracture/matrix block (k). Flux $(\overline{Q})_\Omega^k$ is computed from the flux density vector $(\bar{q})_\Omega^k$ and from the sectional area A_{OUT}^k. The area depends on the shape and orientation of the unit block Ω^k (or its intersection with the upscaling domain: $\Omega^k \cap \Omega$), and on the direction of local flux vector (q^k). It is of the form (cf. Cañamón (2006) for details):

$$(A_{\mathrm{OUT}}^k)_i = \sum_{s=1}^{s=N_k} A_s^k \cdot (n_i)_s^k, \quad (n_i)_s^k = \max((n)_s^k \cdot q_i, 0) \tag{6}$$

where

N_k is the number of faces of the prismatic block number "k" (taking into account only the part of the unit block that intersects the upscaling domain, that is: $\Omega^k \cap \Omega$);

$(n_i)_s^k$ is the ith component of the unit normal vector coming out of face A_s^k, where "s" is the face index;

and

Index "i" (i = 1, 2, 3) indicates Euclidian direction (cartesian axes x_1, x_2, x_3);
Index "k" indicates the unit block number (and the single piece of fracture in it);
Index "s" (s = 1, 2, 3, 4, 5, 6 or more) indicates the sth face of the prismatic unit block.

3.2.2.1. Remark on geometric calculations. The prismatic "unit block" is a 6-faced parallelepiped rectangle if the fracture is rectangular and contained within the upscaling domain. Disc fractures are approximated by octogonal fractures, leading to octogonal prismatic blocks. But block shapes become more complex for those intersecting the upscaling domain boundary. Geometric approximations have been tested to simplify and accelerate such calculations. For instance, when upscaling domains are cubic voxels, it was demonstrated that each cubic domain may be approximated as a sphere without much loss of precision in the geometric superposition calculations.

Now, inserting Eq. (6) into Eq. (5), and using the equivalent Darcy law of Eq. (4) for each unit block Ω^k, we find that the total flux vector obeys a macroscale Darcy law of the form:

$$\left(\overline{Q_i}\right)_\Omega = (K_{ij})_{MF}^{eq(\Omega)} J_j \quad (i = 1,2,3) \tag{7a}$$

with an equivalent macroscale permeability K_{ij}, of the form:

$$(K_{ij})_{MF}^{eq(\Omega)} = \frac{\sum_k^{N_f} \left[\sum_{\theta_{si}} A_s^k \cdot (n_i)_s^k\right] \left[\left(\delta_{ij} - n_i^k n_j^k\right)\left((1-\varphi_F^k)K_M + \varphi_F^k K_F^{ll}\right) + n_i^k n_j^k \left(\frac{(1-\varphi_F^k)}{K_M} + \frac{\varphi_F^k}{K_F^c}\right)^{-1}\right]}{\sum_k^{N_f} \sum_{\theta_{si}} A_s^k \cdot (n_i)_s^k} \tag{7b}$$

where

"N_f" is the total number of fractures located in the upscaling domain Ω;
"k" refers to both fracture (k) and unit block (k), also named Ω_k;
n_i^k is the ith component of the unit vector normal to fracture k;
$(n_i)_s^k$ is again the ith component of the unit normal vector coming out of face A_s^k;
θ_{si} is the cosine angle between normal vector $\mathbf{n}_s^k$ and the unit vector $\mathbf{u}_i$ of axis x_i;
$\varphi_F^k$is the volumetric fraction of single fracture (k) with respect to vol(Ω^k).

3.2.2.2. Remark on the nature of the resulting K_{ij}. Provided simplification of the sectional area term inside the sum (Eq. (7b)), the equivalent permeability K_{ij} becomes a true tensor independent from the direction of the macroscale hydraulic gradient. The relation flux/gradient relation (Eq. (7a)) becomes then linear. The resulting macroscale permeability K_{ij} is then a second rank symmetric tensor. For more details, see for instance Cañamón (2006) and Cañamón et al. (2007).

The entire procedure is implemented in a Matlab program, which visualizes the geometric structure of the EDZ as well as the resulting 3 × 3 K_{ij} tensors as ellipsoïds. A qualitative validation test of the program involving a single large planar fracture is shown in Fig. 6.

Fig. 6 presents a simple test, with a single fracture crossing a low permeability rock matrix. This test was carried out on a 3D cubic domain, but the geometry of the problem is planar (whence the 2D views). The domain is partitioned into cubic voxels used as homogenization sub-domains. Clearly, some voxels remain "intact", i.e., not crossed by the fracture. In the plane view of Fig. 6a, note that four pixels out of nine pixels remain "intact"; on the contrary, the central pixel is entirely crossed by the fracture.

Note that the ellipsoïds represent the information obtained by diagonalizing the 3 × 3 K_{ij} matrix in each voxel. Thus, each ellipsoid represents the equivalent tensorial permeability K_{ij} for the given voxel (they are shown only in plane view, in Fig. 6b). The three diameters of the ellipsoïds are proportional to the three principal permeabilities (eigenvalues), and they are aligned with the three principal axes of permeability (eigenvectors).

In the plane view of Fig. 6b, the central pixel is the most influenced by the fracture (strongest anisotropy ratio). The small spheres represent the small isotropic permeability of the intact rock matrix: they are located in the four outer pixels not crossed by the fracture.

3.2.3. The special case of nonplanar "chevron" fractures: discretization into triangular plane patches

The superposition method was designed initially for systems of planar fractures. However, in the present case, we are also dealing with large 'chevron' shear fractures represented by curved surfaces. The question arises: how to take these curved 'conductors' into account?

In order to continue taking advantage of the simplicity of the superposition approach, we chose to convert each parametric surface into a set of planar 'patches'. The idea is that the previous superposition method can then be applied without much modification to the set of planar patches.

Preliminary tests have shown that triangular patches are preferable to quadrilateral patches, because the resulting quadrangles are nonplanar (while the triangular patches are planar, as required). Therefore, the unit blocks (single fracture/matrix blocks) representing the chevron fractures and their surrounding matrix are triangular prisms. The unit blocks corresponding to these triangular patches can finally be added to the set of all unit blocks pertaining to the different types of conductors, i.e., planar fissures, or else, curved chevron fractures.[1]

The discretization of the curved chevron fractures into triangular plane patches was performed using Matlab functions related to the vizualisation of surfaces in 3D (surf and surf2patch). An example is shown in Fig. 7. Note that this procedure would not have been as easy to implement without a parametric representation of chevron fracture surfaces.

3.2.3.1. Remarks on triangular patches. In Fig. 7, the normal to each triangle is not displayed at the center of the triangle, but rather, at some point used as the local origin, located on one of the edges of the triangle. Indeed, the faceted triangular approximation of the curved chevron surface was performed using the Matlab *surf2patch* function, which defines a local coordinate system (X, Y) with a local origin (0, 0) such that each triangle is partitioned by the Y-axis into two "right angle" triangles. The local Z-axis is normal to the local (X, Y) plane of the triangle.

Also, it may be interesting to note why quadrangular patches were not considered: their four vertices will not be coplanar in general, contrary to the case of triangular simplexes, which are necessarily planar in 3D space (indeed, three vertices are always co-planar).

3.2.4. Sequential upscaling procedures

It has been noted that the above superposition approach comprises intermediate steps, such as the calculation of exact unit

[1] In fact, as will be seen just below, we have finally chosen to treat the fissures/fractures upscaling problem sequentially: first the planar disc fissures, then the large curved chevron fractures.

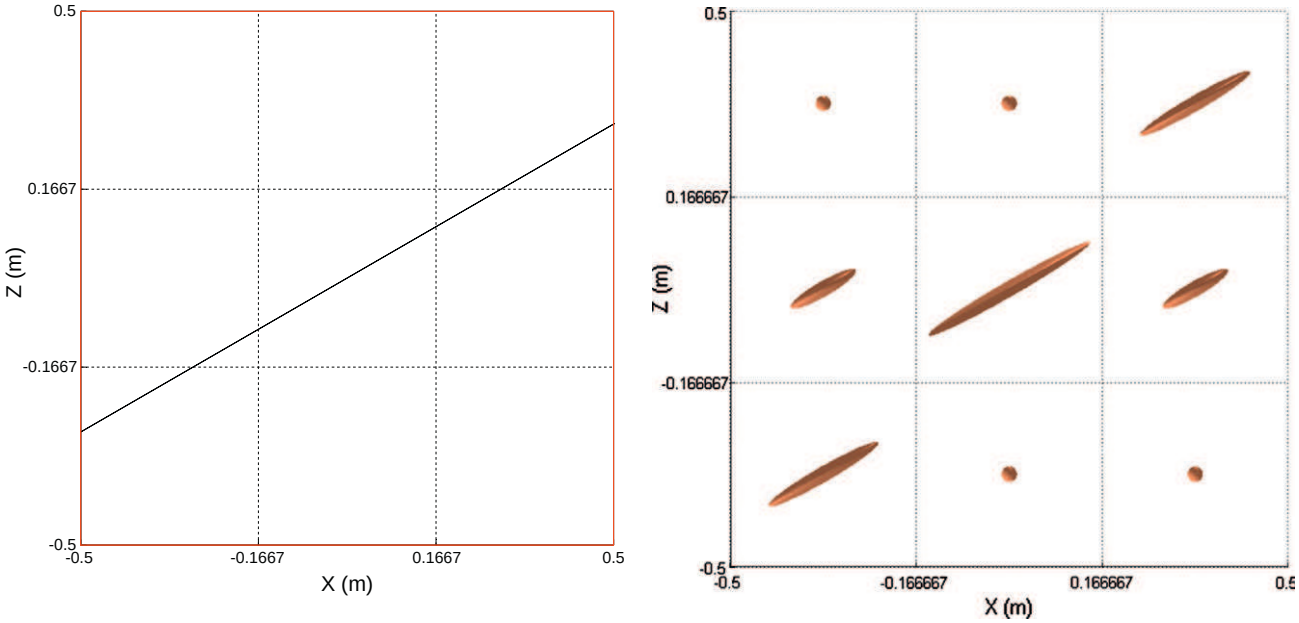

Fig. 6. Test of permeability upscaling by the superposition method. (a) Left: «fractured» medium containing a single large planar fracture. (b) Right: upscaled permeability K_{ij} obtained by the superposition method. The geometry of this test is "2D" due to plane symmetry, but the obtained K_{ij} is still a 3×3 s rank tensor. The K_{ij} tensors are represented by ellipsoïds. The diameters lengths and orientations represent the principal permeabilities (K^*_{ii}) and the principal axes (Xi*) of the K_{ij} tensor.

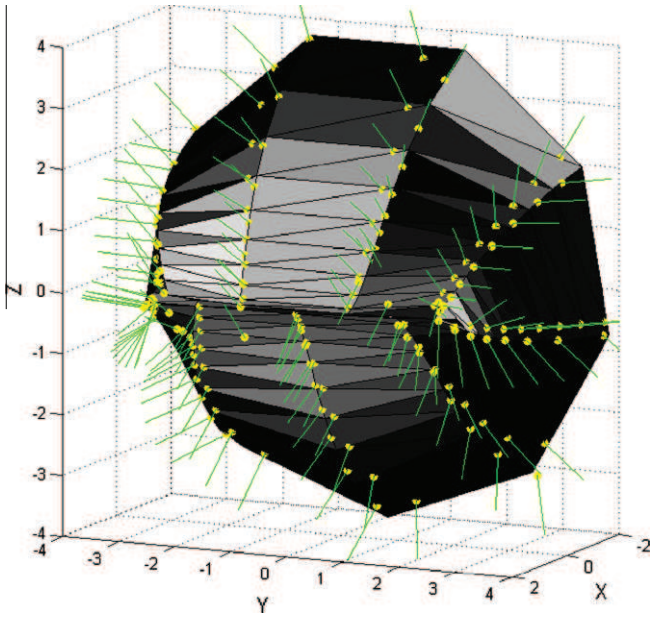

Fig. 7. Approximation of the parametric surface of a 'chevron fracture' into triangular plane patches, showing the patches (greyscale triangle), the nodes (yellow symbols) and the normals (green sticks). The discretization of the surface and the geometric information on patches were obtained using Matlab (and in particular the function '*surf2patch*').

block permeability tensors. The method is therefore sequential in the following sense:

- Sequential upscaling: K_{ij}(UnitBlocks) → K_{ij}(UpscalingDomain)

In addition, as will be seen, other sequential procedures are used for application to the specific problem of the fissured + fractured Excavation Damaged Zone around a cylindrical drift:

- Sequential upscaling: K_{ij}(3D) → K_{ij}(2D) → K_{ij}(global)
- Sequential upscaling: upscaling results (macro-permeability tensors)

Hydraulic upscaling was carried out on the 20 m × 13 m × 13 m domain, comprising the 20 m long stretch of annular 'EDZ', using a partition of upscaling cells (voxels) of size $\Delta x = \Delta y = \Delta z = 0.50$ m (cubic voxels), leading to a total of $40 \times 26 \times 26 = 27{,}040$ upscaling voxels (including the unused voxels located inside the drift).

Note. The upscaling domains (voxels) may contain several or many fractures, and they should not be confused with the "unit blocks" of the superposition method. The unit blocks are prismatic polygonal blocks made up of a single piece of fracture plus the surrounding matrix (unlike the voxels, unit blocks are positioned and oriented in space like the fractures to which they are closely associated).

The chosen size $(0.5\text{ m})^3$ of the upscaling blocks (voxels) was chosen based on a combination of criteria. First, voxel size was chosen on the same order as chevron spacing (in fact it is exactly the same: 0.5 m) so that, after performing 3D upscaling, each chevron fracture can still be "seen" in terms of the 3D K_{ij} distribution. Secondly, we had to account for the strongly inhomogeneous density of fissures: smaller voxels would yield noisy distributions of K_{ij}, and coarser voxels would completely hide the radial inhomogeneity of the EDZ in terms of K_{ij}.

The statistical fissures, and the periodic set of curved "chevron" fractures, were treated separately in order to assess their relative influence. In what follows, we consider first the statistical set of disc fissures, then the nonplanar "chevron" fractures. A sequential upscaling procedure is used to obtain the macro-permeability of the complete system ('matrix + fissures + chevrons') – as explained in the previous section.

4.1. EDZ macro-permeability K_{ij}: matrix/fissures system. We consider here the *set of* 10,000 *random 'fissures'* embedded in the intact porous matrix. The hydraulic conductivity of the *intact matrix* is assumed to be isotropic and equal to:

$K_M = 0.5E-12$ m/s.

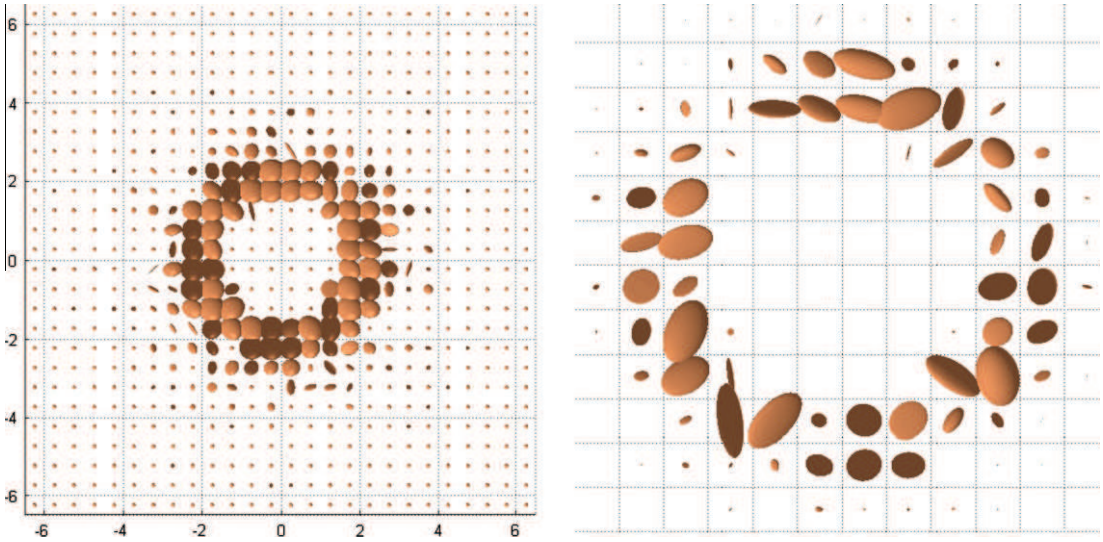

Fig. 8. *Upper left*: Transverse view of permeability ellipsoïds in the first transverse plane $i = 1$ ($x \approx 0$) across the EDZ. The square mesh represents upscaling windows (cubic voxels of side 0.5 m); in this transformed ln K view, aspect ratios and anisotropy ratios are not conserved: ellipsoïd diameters are proportional to ln K_{ii}^*. *Upper right*: zoom of the same transverse view (near the gallery wall), but without the ln K transform: here, aspect ratios and anisotropy ratios are conserved, because ellipsoïd diameters are proportional to K_{ii}^*.

Let us first discuss the question of the assumed isotropy of the "matrix". Initially, it was planned to account for matrix anisotropy, or "microscale" anisotropy. However, in retrospect, we finally decided to implement upscaling with matrix isotropy for several reasons:

- Laboratory measurements of permeability K in the undisturbed *Callovo-Oxfordian Argilite at Bure* indicate that K is only moderately anisotropic at the "microscopic" scale of lab samples (e.g. 1–10 cm scale): horizontal K is at most 10 times the vertical K (e.g. 5×10^{-13} m/s and 5×10^{-14} m/s respectively); for a precise reference, see p. 202 in ANDRA's (2005) "Dossier Argile".
- It will be seen in the next section that the upscaled permeability obtained with chevron fractures (*matrix + fissures + chevrons*) is strongly anisotropic at the local scale of 0.5 m voxels (mesoscale). Therefore, the moderate anisotropy of the matrix is not crucial in terms of practical results.
- Furthermore, a theoretical motivation leads us to avoid putting anisotropy in the "matrix" (this is perhaps more subtle, and debatable). It is motivated by the requirement that the whole upscaling approach should be consistent in terms of scales. In the so-called "intact" matrix, microstructures exist due to tectonic history and stress anisotropy. But, in our upscaling approach, we consider up to 10,000 statistical fissures: that is approximately 1000 fissures in-between 2 chevron fractures. These random objects range from moderate size fractures to micro-fissures (very small diameters and apertures). Thus, rather than using a locally anisotropic "matrix", a more consistent approach could be to better represent the anisotropic statistical geometry of the micro-texture, with the aim of better reproducing (via upscaling) the anisotropy observed at the scale of small lab samples.

Now, given the assumed matrix permeability above, the results presented in this section concern the spatial distribution of the upscaled permeability tensor (K_{ij}) obtained for the *matrix + fissures* system by the superposition method (the next section will consider the chevron fractures). These *matrix + fissures* results are shown in the following Figs. 8–10:

- Fig. 8 shows a front transverse view of the macro-permeability tensor K_{ij} at the entrance of the gallery, where K_{ij} was obtained by upscaling over a 3D grid of cubic 'voxels' of size 0.5 m. Since K_{ij} is a 3×3 tensor, it is represented as ellipsoïds.
- Fig. 9 shows another view of the same macro-permeability tensor K_{ij}, upscaled over a 3D grid of cubic 'voxels' of size 0.5 m: this time the spatial distribution of K_{ij} is shown in 3D by looking at a longitudinal vertical mid-section cut of the gallery.
- Fig. 10 shows the transverse distribution of the upscaled "2D" permeability tensor, obtained from the previous 3D distribution $K_{ij}(x, y, z)$ with a second upscaling, namely, by averaging $K_{ij}(x, y, z)$ along the axial direction of the drift (length $L_x = 20$ m). The resulting macro-$K_{ij}(y, z)$ corresponds to a window size 0.5 m $\times$ 0.5 m $\times$ 20 m.

To obtain these results, the superposition method was applied sequentially from higher to lower dimensional results. The detailed spatial distribution of K_{ij} was first obtained in 3D space, over a grid of homogenization voxels ($\underline{\boldsymbol{x}}_{IJK}$). The permeability was then further upscaled along the axis of the gallery to obtain a 2D transverse distribution of K_{ij}, and then it was upscaled again by averaging in the remaining directions to obtain a global K_{ij} tensor for the whole 'EDZ'. This procedure can be viewed as *sequential upscaling across dimensions*:

- upscaling is first performed over cubic blocks to obtain the block-scale K_{ij}'s in 3D;
- then, based on the previous result, upscaling is performed again over elongated parallelepipeds having the length of the entire drift, to obtain a 2D transverse distribution of K_{ij}'s;
- finally, using previous results, upscaling is conducted over the whole annular 'EDZ' region to obtain a global value of K_{ij}.

As can be seen in the figures, the block-scaled 3D and 2D equivalent K_{FISSURES} have a radially inhomogeneous distribution in space, similar to the inhomogeneous statistics of the fissures. At the global scale of the EDZ, the equivalent permeability tensor for the *matrix + fissures* is:

$$(\underline{\underline{K}})^{\text{EDZ}}_{\textit{fissures}} \approx 2.8 \times 10^{-9} \delta_{ij} (\text{m/s}) \quad \text{where } (i,j) = 1,2,3. \tag{8}$$

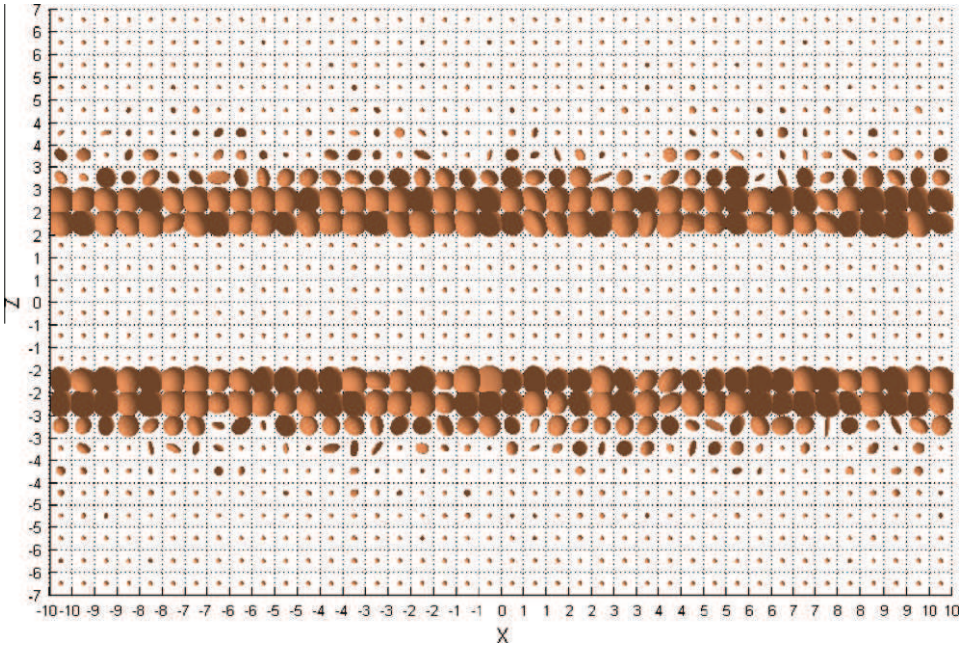

Fig. 9. Longitudinal view of permeability ellipsoïds in the central vertical plane ($y \approx 0$, slice $j = 13$). The log-transform ln K is used here, so aspect ratios and permeability anisotropy ratios are not conserved (i.e., diameters are proportional to ln K_{ii}^* rather than K_{ii}^*).

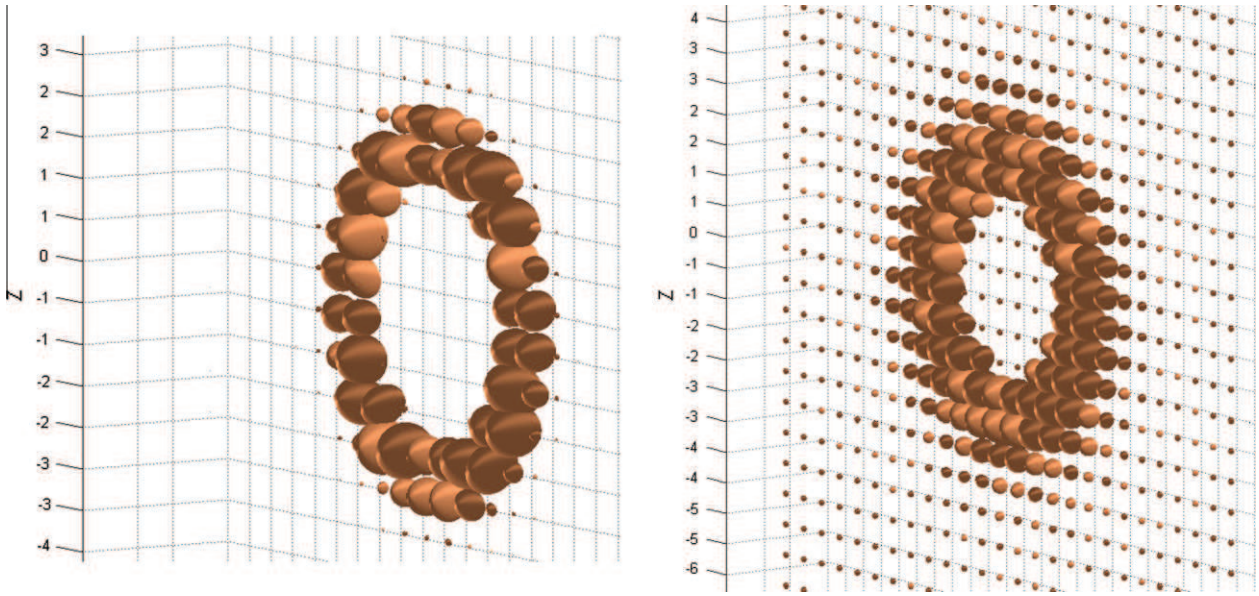

Fig. 10. Transverse distribution of upscaled "2D" permeability tensor : perspective view of 3×3 permeability ellipsoïds, with log-transform (ln). This planar distribution $K_{ij}(y, z)$ $(i, j = 1, 2, 3)$ was obtained by averaging or upscaling the 3D macro-$K_{ij}(x, y, z)$ through the axial direction of the drift (length $L_x = 20$ m). The upscaling window size of the resulting K_{ij} is 0.5 m $\times$ 0.5 m $\times$ 20 m. *Left*: aspect ratios and permeability anisotropy ratios are conserved (ellipsoïds principal diameters are proportional to K_{ii}^*). *Right*: another view using log-transform (ln K); here, ellipsoïd diameters are proportional to $\ln(K_{ii}^*)$, so that permeability aspect ratios are not preserved here (contrary to the left view).

The resulting tensor is nearly isotropic, as expected, due to the isotropic orientations of the statistical set of planar disc fissures. The magnitude of the equivalent permeability due to fissures (K_{FISSURES}) is roughly 5000 times larger than the intact matrix permeability (K_M).

4.2. EDZ macro-permeability K_{ij}: matrix + fissures + chevrons.

Finally, the entire system comprising the *matrix + fissures + chevron fractures* was upscaled sequentially as follows:

- matrix + fissures → K_{ij} (matrix + fissures) from previous step
- homogenized K_{ij}(matrix/fissures) + chevrons → K_{ij}

In addition, a sequential procedure was also used, as before, to obain the "2D transverse" distribution of K_{ij} from the "3D upscaled" K_{ij}:

- upscaling over a 3D grid of 'voxels' → $K_{ij}(x_{IJK}, y_{IJK}, z_{IJK})$ → averaging axially → $K_{ij}(y_{JK}, z_{JK})$

The resulting spatial distributions of the equivalent macro-permeability K_{ij} (3×3) in 3D and in 2D are displayed in Figs. 11–13(a and b).

A remarkable feature is the way the tensorial block-scale permeabilities $K_{ij}(x, y, z)$ are distributed in space. It is clear that the equivalent K_{ij}, due to the large chevrons fractures, are highly

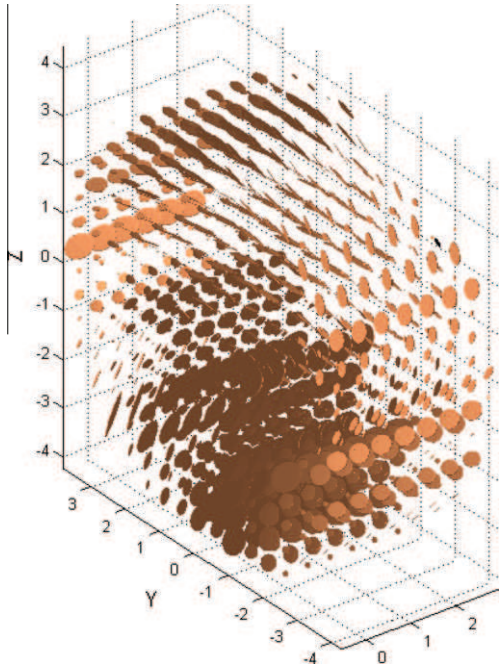

Fig. 11. Perspective view of '3D' matrix + fissures + chevrons macro-permeability tensors K_{ij} (3×3) distributed on a 3D grid of voxels over a 3.5 m stretch of the drift (EDZ). NB: in this view, the principal diameters of the ellipsoïds are proportional to principal permeabilities (aspect ratios preserved).

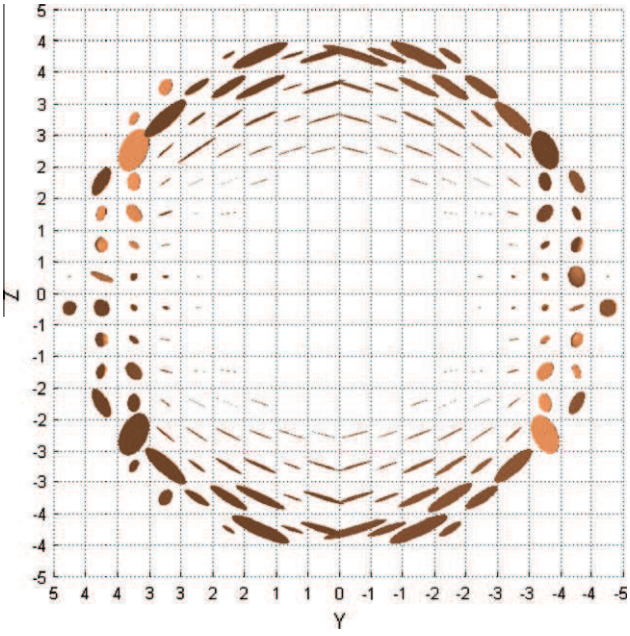

Fig. 12. Plane view of '2D' matrix + fissures + chevrons macro-permeability tensors K_{ij} (3×3) distributed on a 2D grid of pixels, obtained by upscaling 3D permeability tensors axially along the 20 m long drift. NB: principal diameters are proportional to principal permeabilities (aspect ratios are preserved).

anisotropic, with spatially variable principal directions, locally aligned with the tangent plane to the fracture surface (as can be seen from all Figs. 11–13). The effects of individual chevron fractures are clearly visible in the detailed 3D block-scale K_{ij}, because the block size was chosen just equal to the interspacing of the periodic set of chevron fractures.

The 'global K_{ij}' permeability of the system at the scale of the entire EDZ was computed tentatively: the resulting global tensor is weakly anisotropic (ratio $K_{zz}/K_{xx} \sim 3/8$), much less so than the local block scale K_{ij}'s. Its magnitude was evaluated using a spherical norm to be roughly about $K(global) \sim 5.0E-5$ m/s. However, admittedly, the EDZ global permeability K_{ij} due to chevrons...lacks physical meaning, especially as a tensorial quantity, given the radially inhomogeneous distribution of voxel-scale K_{ij}'s. This radial inhomogeneity is itself due clearly to the diverging geometry of chevron fractures around the drift.

Let us focus solely on the magnitude of the 'global' K_{ij}. Recall that, in this work, the chevron fractures were assumed to have a constant hydraulic aperture $a = 100\ \mu m = 1.0\,E-4$ m. In reality, however, it is expected that aperture decreases with radial distance from the drift wall. Furthermore, it is well known that permeability tensors are very sensitive to aperture 'a', owing to the so-called "*cubic law*". This can be made clear for the case of a parallel set of infinite planar fractures; the equivalent permeability along any direction in the plane of the parallel fractures is (Ababou, 1991, 2008):

$$K = (g/12v)(a^3/\lambda) \quad (\mathrm{m/s}) \tag{9}$$

where λ is fracture inter-spacing and v is water's kinematic viscosity (m^2/s). Thus, decreasing aperture 'a' by a factor 10 (say $a = 10\ \mu m$ instead of 100 μm) will decrease the equivalent permeability due to chevron fractures by a factor 1000 (say $K = 5.0E-8$ m/s instead of $K = 5.0E-5$ m/s). This example makes it clear that the equivalent permeability induced by the periodic set of (large) chevron fractures alone, is very sensitive to their assumed hydraulic aperture. The permeability due to 'chevrons', with assumed hydraulic aperture 100 μm, is about 4 orders of magnitude larger than that due to statistical fissures – but becomes only 1 order of magnitude larger with a hydraulic aperture of $a = 10\ \mu m$ instead of 100 μm. Clearly, this is due to several factors, geometric as well as hydraulic: the large extent of chevron fractures; the constant aperture assumption; and the cubic law behavior (assuming Poiseuille flow in the fractures).

5. Upscaling along boreholes: comparisons with in situ data

A different averaging procedure was used to compare the upscaled permeabilities with observed permeability profiles from *in situ borehole tests*.

For this purpose, the superposition method was applied to *moving windows along a given line of points*, rather than to a fixed partition of cells.

As an example, let us consider again here the *matrix + fissures system* (which comprises both planar microfissures and also, particularly near the drift wall, somewhat larger planar fractures of submetric size).

After upscaling the permeability along moving spherical windows, we obtained synthetic permeability profiles $K(r)$ along so-called *'numerical boreholes'*. These are compared to actual borehole permeability profiles in Fig. 14a, as explained in the figure caption.

The "fit" in Fig. 14a appears quite good, considering the many uncertainties in the system. This encouraging result confirms the choice of statistical properties, and in particular, the chosen decrease of mean density, aperture and diameter with radial distance from the drift wall (see earlier, Section 2.1). In fact, this set of geometric properties can be viewed as the solution of an inverse problem, solved here by trial and error. It is probably nonunique, although we hope our result is a relatively robust sub-optimum. Here are a few more details.

- The "adjusted" parameters were the statistics of the diameters and the decreasing density of fissures. The best results were obtained with a volumetric density of fissures $\rho \sim 1/r^{3/2}$ where "r" is the distance from the drift wall. By geometric probability arguments, the corresponding PDF of radial positions of the random fissures must decrease like

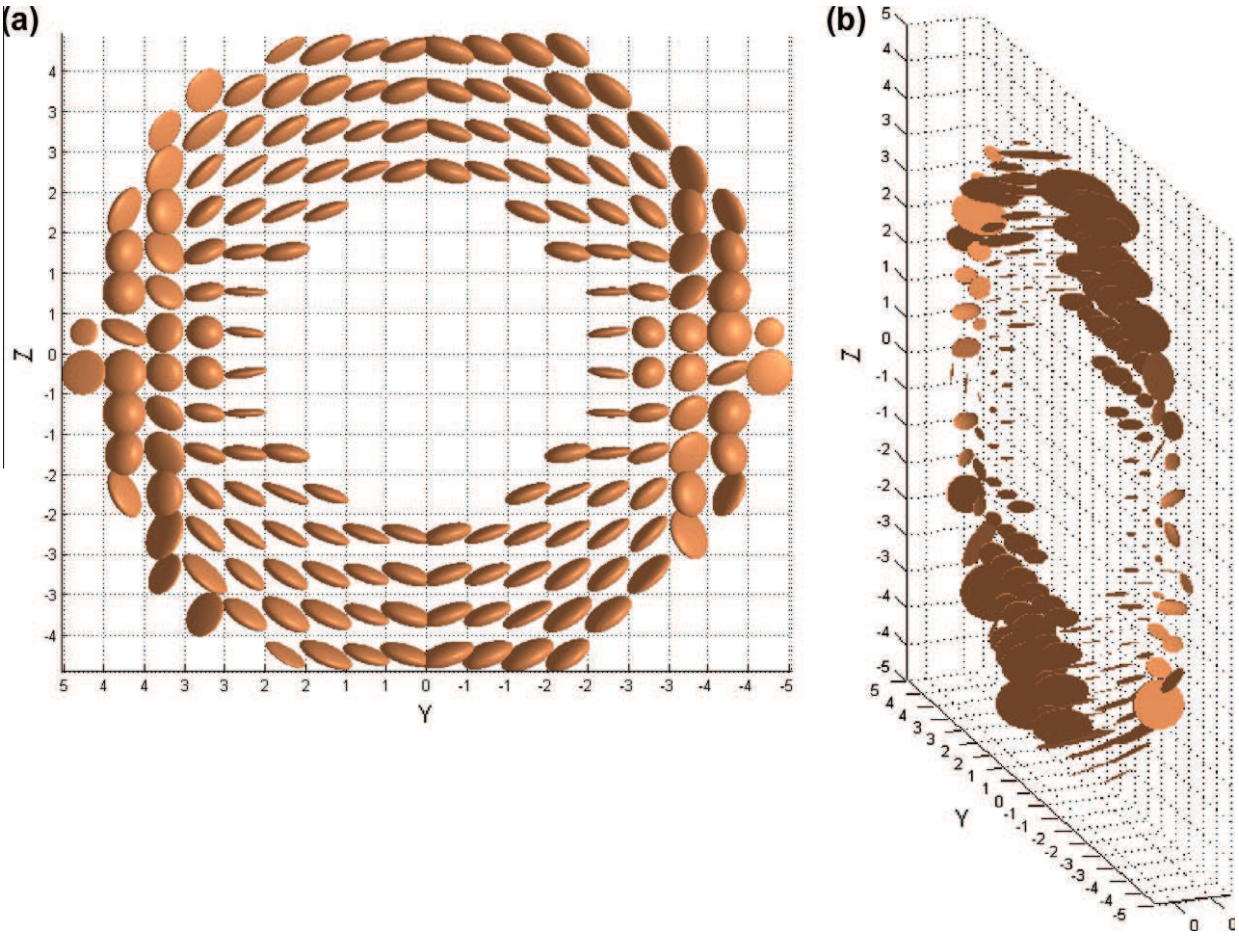

Fig. 13. (a and b). Result of '2D' hydraulic upscaling for the complete system (matrix + fissures + chevron fractures). Above (a): plane view of equivalent permeability ellipsoïds K_{ij} (3×3) distributed on a transverse 2D grid of 'pixels'; in this view, a logarithmic scale is used for the principal diameters of the ellipsoïds (they are not proportional to principal permeabilities, and permeability aspect ratios are not preserved graphically). Right (b): another plane view of the same equivalent permeability ellipsoïds K_{ij} (3×3) distributed on a transverse 2D grid of 'pixels'; in this view, the logarithmic scale is not used (the principal diameters are proportional to principal permeabilities, and aspect ratios are preserved).

$f \sim 1/r^{1/2}$. On the other hand, assuming a constant radial PDF ($f \sim f_o$) corresponds to a volumetric density that decreases as $\rho \sim 1/r$. From our trial and error tests, we found that the $\rho \sim 1/r$ decrease was too slow to reproduce correctly the permeability borehole profiles, compared to $\rho \sim 1/r^{3/2}$ which gave better results (see Appendix A).

We used a fairly large mobile window, a sphere of diameter 0.75 m. Indeed, smaller window diameters induced oscillations not observed in the actual borehole measurements.

- Admittedly, if the 3D domain of influence of the borehole permeability measurements were exactly known, it should be used as the moving window. But it is quite difficult to obtain a reliable and stable evaluation of the domain of influence of measurement in the presence of fissures and fractures. According to our results, the cylindrical borehole test interval greatly underestimates the true domain of influence of the measurement. Therefore, we used instead a "neutral" spherical window, and we chose for its diameter the value that produced the best numerical profiles compared to experimental profiles.

The large "chevron" fractures were not taken into account in the numerical boreholes of Fig. 14a. Given their 3D curved shapes and their interspacing (supposedly 0.5 m axially), the chevron fractures may intersect radial boreholes at various distances. These distances can be theoretically calculated from our surface model. However, geometric uncertainties exist due to the fact that the actual shapes of "chevrons" are less regular than the proposed parametric surfaces. And there are other uncertainties due to their unknown aperture distribution. Indeed, chevron aperture was assumed constant in this work, but an alternative hypothesis is that aperture decreases away from the drift wall. As a consequence, individual chevron fractures may or may not have a visible effect on measured $K(r)$ profiles *in situ*.

For all these reasons, numerical borehole tests were developed separately to investigate the effects of chevron fractures (at most three of them) intersecting a radial horizontal borehole at various distances.

One of these tests is shown in Fig. 14b. It includes the statistical fissures as well as three large chevron-type fractures. In fact, a comparison is made "with or without" chevrons, using the same spherical window size in both cases (diameter 0.75 m). With "chevrons", a local maximum of $K(r)$ is observed at distances 0.75–1.25 m from the drift wall; the permeability profile is nonmonotonous, and permeability can be up to 2 orders of magnitude higher with the "chevrons" than without "chevrons" (locally). Beyond 2 m from the drift wall, however, the chevrons have no effect on $K(r)$.

These comparisons (Fig. 14b) are based on numerical borehole calculations; they could not have been deduced directly from *in situ* measurements.

6. Conclusions and outlook

In this work, we have developed:

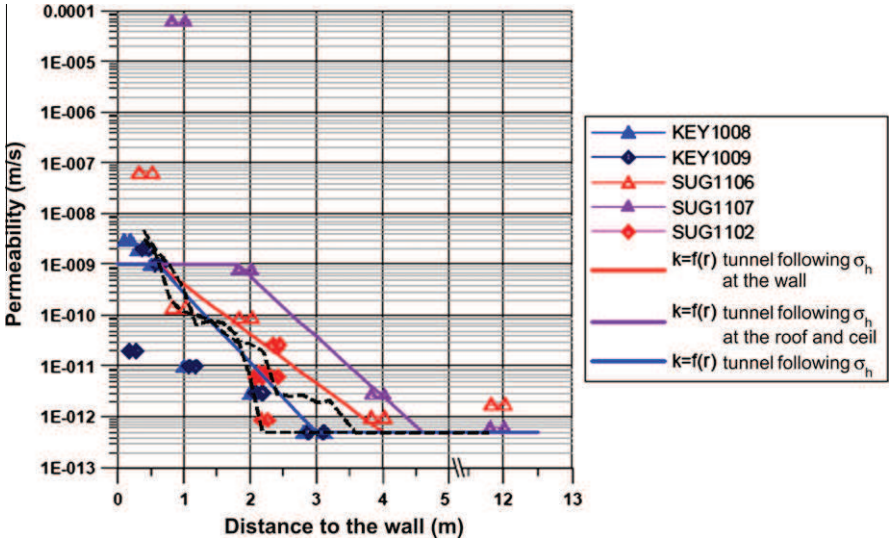

Fig. 14a. Radial profiles of permeability $K(r)$ measured in the GMR tunnel at Bure (from Fig. 12 of Armand, 2007), and comparison with 2 homogenized permeability profiles $K(r)$ (the superimposed *black dashed curves* – – – –). The latter were computed for the matrix + fissures system (with 10,000 random fissures) using a moving window along the borehole line ('numerical borehole'). The "upper" dashed line gives $K(r)$ along a horizontal borehole (in the left wall of the tunnel), and the "lower" dashed line gives $K(r)$ along a vertical borehole (at the roof of the tunnel). The mobile window is a sphere of diameter 0.75 m. The resulting $K_{ij}(r)$ is a 3×3 anisotropic tensor, although only its norm $K(r)$ is plotted here (Frobenius norm: geometric mean of the three principal components).

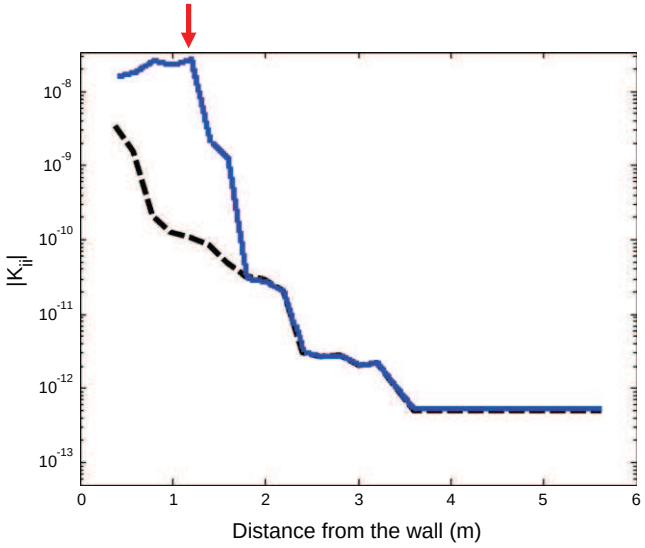

Fig. 14b. Comparison of two numerical $K(r)$ profiles along a horizontal radial borehole *with*/*without* three large chevron-type fractures intersecting it (this sensitivity test is actually performed with three large disc shaped fractures mimicking three chevron fractures intersecting the borehole). The dashed black curve is the profile "without chevrons", and the solid blue curve is "with chevrons". The plotted quantity $K(r)$ is the Frobenius norm of K_{ij}. The medium comprises the permeable rock matrix, the statistical system of 10,000 fissures as described in the text, and the three large fractures emulating the chevrons (their aperture is 100 μm; their spacing is 0.5 m along the drift axis; they form an angle 45°/drift axis, and their extent is 1 m away from the drift wall). Both $K(r)$ profiles were computed using the same spherical window of diameter 0.75 m.

- a morphological model of fissured + fractured rock (EDZ) around a cylindrical drift, using concepts from differential geometry (chevron fractures) and "geometric probability" (statistical set of 10,000 plane disc fissures with radially inhomogeneous properties in 3D);
- a set of sequential procedures for hydraulic upscaling of the fissured and fractured EDZ, based on a (suitably generalized) flux superposition approach.

These methods are applied to the Bure clay rock site (specifically, the GMR drift is used as a template for this study). As a result, we have obtained the macro-permeability of the EDZ in the form of spatially distributed 3×3 K_{ij} tensors over various supports and grids:

- '3D' K_{ij} over a grid of voxels,
- '2D' K_{ij} over a transverse grid of pixels,
- '1D' linear profiles $K_{ij}(r)$ along radial 'boreholes' (the scalar norm $K(r)$ was analyzed),
- '0D' or 'global' K_{ij} value for the entire EDZ (this global value is meaningful only for the subset of isotropic fissures, not for the chevrons fractures, as pointed out earlier).

The results obtained indicate that. . .:

- As can be seen in the figures, the 3D and 2D equivalent K_{FISSURES} have a radially inhomogeneous distribution in space, similar to the inhomogeneous statistics of the fissures.
- The magnitude of the equivalent permeability due to fissures (K_{FISSURES}) is roughly 5000 times larger than the intact matrix permeability (K_M).
- The tensorial permeabilities $K_{ij}(x, y, z)$ calculated at voxel-scale for the fissures + chevrons system have a remarkable distribution. They are highly anisotropic. Their principal directions are clearly aligned locally with the tangent plane of chevron fractures (as can be seen from Figs. 11–13). The effects of individual chevron fractures are clearly visible in the 3D distribution of voxel-scale K_{ij}'s, because voxel size was chosen equal to chevron spacing.
- A global permeability K_{ij} for the fissures + chevrons system was obtained from the voxel-based K_{ij} distribution (over the whole EDZ). This global K_{ij} appears only weakly anisotropic. However, admittedly, it lacks physical meaning – especially as a tensorial quantity – because of the radially inhomogeneous distribution of the voxel-scale tensors K_{ij}'s. The latter is clearly due to the diverging geometric structure of the chevron fractures around the drift.
- Nevertheless, it is useful to consider the norm K of the global tensor K_{ij} (for the whole EDZ). It is found that the permeability due to 'chevrons' is about 4 orders of magnitude larger than that due to statistical fissures – if the hydraulic aperture of chevrons is 100 μm. But by a simple argument, it

would become only 1 order of magnitude larger if the hydraulic aperture of chevrons were taken 10 μm instead of 100 μm. This sensitivity is due to several factors, geometric as well as hydraulic: large extent of chevron fractures; constant aperture assumption; and cubic law behavior due to the assumption of Poiseuille flow in fractures.

The upscaled permeabilities K_{ij} obtained in this work can be used for large scale flow simulations in any simulation code that accepts Darcy's law with a spatially variable, full permeability tensor $K_{ij}(\mathbf{x})$. Furthermore, the piecewise constant block-by-block evaluations of equivalent tensors $K_{ij}(\mathbf{x}(i_X, i_Y, i_Z))$ can be replaced by more continuous distributions of $K_{ij}(\mathbf{x})$ obtained by the 'moving window' procedure as examplified in the study of the last section on numerical *vs.* experimental boreholes.

In the near future, we plan to implement or study the following features.

- Evaluate other useful alternative definitions for the full K_{ij} tensor, taking into account more directly the specific annular structure of the fissured/fractured EDZ at Bure. Indeed, while the heterogeneous structure of the EDZ is not exactly cylindrical, it may still be useful to define radial and tangential upscaled permeabilities; these should be defined properly from directional versions of Darcy's law, and the relation between cylindrical and cartesian upscaling should be clarified as well.
- Extend the numerical borehole concept, and investigate more systematically the inverse problem aimed at identifying optimal geometrical characteristics and hydraulic apertures for the different sets of fissures and fractures;
- Study the equivalent behavior of the EDZ for other hydrodynamic phenomena such as unsaturated flow and more generally two-phase flow;
- Extend the homogenization method to hydro-mechanical processes in the EDZ: this leads to spatially distributed macroscale 4th rank tensorial stiffnesses and Biot coupling coefficients.

In closing, let us briefly discuss some issues related to the hydraulic behavior of the 'EDZ' under partially saturated/unsaturated conditions, currently under study based on Darcy–Buckingham's law with pressure-dependent permeability:

- In the presence of fissures and other heterogeneities, unsaturated rock can behave in a complex way, due to the interaction between nonlinearity and spatial variability of coefficients (permeability and moisture content).
- For example, damaged zones or fissured zones can act either as capillary barriers or as conductors, depending on the state of water pressure or moisture content.
- At macro-scales, moisture-dependent or pressure-dependent anisotropy can arise, and therefore, the equivalent permeability becomes a nonlinearly anisotropic function of pressure.

To study these phenomena, the present results on the equivalent saturated permeability tensor will be useful, although a somewhat different approach will also be needed in order to capture the equivalent nonlinear anisotropic behavior of the relative permeability–pressure curve.

Acknowledgments

This work was conducted at IMFT (Institut de Mécanique des Fluides de Toulouse, France), in collaboration with ANDRA (Agence Nationale de Gestion de Déchets Radioactifs, France), in the framework of a research project funded by ANDRA (contract ANDRA 040179): "*UPS4 – Simulation Mécanique: élaboration des modèles mécaniques et hydromécaniques homogénéisés de l'EDZ au champ proche d'un ouvrage de stockage*". The first author acknowledges the contribution of Dr. David Bailly (then post-doctoral researcher at IMFT) on 3D visualization issues and upscaling algorithms related to this work. Finally, the authors wish to thank the two anonymous reviewers for their helpful comments and suggestions, which have brought about significant improvements in the final version of this paper.

Appendix A. Probability analysis of discrete fissures in cylindrical geometry: calculation of volumetric density $\rho(r)$ and other radially inhomogeneous statistics

The purpose of this Appendix A is to establish a relation between the Probability Density Function (PDF) of the euclidian positions (x, y, z) and the radial positions (r) of the centers of planar disc fissures, where (x) is parallel to the axis of the cylindrical drift, and $r = \sqrt{(y^2 + z^2)}$. The euclidian volumetric density of fissures $\rho_{03}(r)$ or $\rho(r)$ versus radial distance is thus obtained. Indeed, one needs to be able to specify or to "control" analytically $\rho(r)$.[2] The relations obtained in this appendix helped guide our choice for the statistically inhomogeneous distributions of fissure centers, diameters and apertures in the annular EDZ – all radially decreasing away from the drift (cf. related Appendix B).

The specification of $\rho(r)$ comprises two steps:

- Step 1. Inhomogeneous radial positions: obtaining PDF $f_R(r)$ by transforming a uniform variable U

To generate multiple replicates of random radial positions (R), we transform the replicates of a uniformly distributed random variable (U). Here, we choose a relation of the form $R = a + b \cdot U^2$, where U is a uniformly distributed random variable on [0, 1]. It is "easier" to generate U with a well chosen congruential random number generator, than to generate R directly. In the case at hand, we can even deduce analytically the PDF of radial positions $f_R(r)$, and we find $f_R(r) \sim 1/\sqrt{r}$ (see below).

- Step 2. Inhomogeneous euclidian positions: relating euclidian PDF $f_X(x)$ to radial PDF $f_R(r)$.

Once the radial PDF $f_R(r)$ is given, it remains to be seen how the euclidian PDF $f_{\underline{\mathbf{X}}}(\underline{\mathbf{x}})$ is related to $f_R(r)$. The euclidian PDF $f_{\underline{\mathbf{X}}}(\underline{\mathbf{x}})$ is the PDF of euclidian positions (x, y, z) of fissure centers. For example, we know that $f_{\underline{\mathbf{X}}}(\underline{\mathbf{x}})$ must be uniform in (x, y, z) space if we want the volumetric density $\rho(r)$ to be uniform, homogeneous, constant in space. In other words: $f_{\underline{\mathbf{X}}}(\underline{\mathbf{x}})$ uniform $\Rightarrow \rho(r)$ constant.

A.1. Specification of the radial PDF $f_R(r)$ by transforming uniformly random positions. In the main text of this paper, we have generated a synthetic system of 10,000 random fissures in the annular EDZ region around a cylindrical drift. This was done by generating the radial transverse positions $r = \sqrt{(y^2 + z^2)}$ of fissure centers using the following transform (see Table A.1):

$$r^{(i)} = R_{\mathrm{TUNNEL}} + (R_{\mathrm{EDZ}} - R_{\mathrm{TUNNEL}}) \times (U^{(i)})^2 \quad \text{where } r = \sqrt{(y^2 + z^2)} \tag{A11}$$

where 'U' is a random variable, uniformly distributed in the [0, 1] interval. To deduce the PDF dénotée $f_R(r)$ of radial positions 'r', we use the classical technique of derived distributions (cf. Papoulis and Pillai, 2002), whence the result:

$$f_R(r) = \begin{cases} \dfrac{1}{2(R_{\mathrm{EDZ}} - R_{\mathrm{TUNNEL}})\sqrt{\frac{r - R_{\mathrm{TUNNEL}}}{R_{\mathrm{EDZ}} - R_{\mathrm{TUNNEL}}}}} & \text{if } r \in [R_{\mathrm{TUNNEL}}, R_{\mathrm{EDZ}}] \\ 0 & \text{else} \end{cases} \tag{A12}$$

[2] Note. The volumetric density of fissures $\rho_{03}(r)$ used in this appendix, also denoted '$\rho(r)$', represents the mean number of fractures per unit volume of space. It should not be confused with the radial linear density $\rho_R(r)$ *(not used here)*. On the other hand, the radial PDF $f_R(r)$ is defined in this Appendix.

This PDF diverges when $r \to R_{\text{TUNNEL}}$, however, the corresponding Cumulated Distribution Function (CDF) $F(r) = \text{Proba}(R \leqslant r)$ does not diverge. Indeed, integrating the PDF, we obtain:

$$F_R(r) = \begin{cases} 0 & \text{if } r \leqslant R_{\text{TUNNEL}} \\ \sqrt{\frac{r - R_{\text{TUNNEL}}}{R_{\text{EDZ}} - R_{\text{TUNNEL}}}} & \text{if } r \in [R_{\text{TUNNEL}}, R_{\text{EDZ}}] \\ 1 & \text{if } r \geqslant R_{\text{EDZ}} \end{cases} \quad \text{(A13)}$$

In particular, we can use this probability law to find the median radial distance of the random fissures $r_{(50\%)}$ such that $F = 0.50$. That is, $r_{(50\%)}$ is such that 50% of the fissures are located at a distance $R_{\text{TUNNEL}} \leqslant r \leqslant r_{(50\%)}$. We find here:

$$R_{(50\%)} = R_T + (R_{\text{EDZ}} - R_T)/4 = 2\text{ m} + (6\text{ m} - 2\text{ m})/4 = 3\text{ m}, \ldots \quad \text{(A14)}$$

which corresponds in fact to:

$$d_{(50\%)} = 1\text{ m}, \quad \text{(A15)}$$

in terms of radial distance '*d*' relative to the drift wall. So, in our model, 50% of the fissures are located within the first meter from the drift wall (inner annular region of the EDZ).

A.2. Obtaining and controlling the euclidian PDF $f_{XYZ}(x, y, z)$ given the radial PDF $f_R(r)$. As noted earlier, given knowledge of the radial PDF $f_R(r)$, one should be able to deduce the PDF $f_{\underline{\mathbf{x}}}(\mathbf{x})$ of fissures positions in euclidian space (x, y, z), from which one should obtain the inhomogeneous volumetric density of fissures $\rho(x, y, z)$ or $\rho(r)$.

Briefly, we have obtained the following result based on geometric probability calculations conducted in cylindrical coordinates (r, θ, x), with the following definitions:

- Define a cylindrical annular region:

$$r = \sqrt{y^2 + z^2} \in [R_{\text{MIN}}, R_{\text{MAX}}]; \quad \theta \in [0, 2\pi]; \quad x \in [0, L] \quad \text{(A16)}$$

- Define a surface element $d\Sigma$ located at radial distance '*r*': $d\Sigma = r d\theta\, dx$
- Define a volume element $d\Omega$ located at radial distance '*r*': $d\Omega = r dr\, d\theta\, dx$

The case of a constant volumetric density ρ_0 is obtained by imposing:

$$dF(r, \theta, x) \equiv \Pr\{(x, y, z) \in d\Omega\} = \text{constant} \times d\Omega \quad \text{(A17)}$$

where the «constant» is precisely ρ_0. It is then easily deduced that, to obtain this constant density requires a *nonuniform* joint PDF of *cylindrical positions* (r, θ, x). Calculations show that this PDF depends only on '*r*', and more precisely, it is found to be exactly as follows:

$$f_{R,\Theta,X}(r, \theta, x) = f_R(r) = \frac{1}{2\pi} \times \frac{1}{L} \times \frac{2r}{\left(R_{\text{MAX}}^2 - R_{\text{MIN}}^2\right)} \text{ si } R_{\text{MIN}} \leqslant r \leqslant R_{\text{MAX}}, \quad \text{et } f_R(r) = 0 \text{ sinon.} \quad \text{(A18)}$$

In conclusion:

- To obtain a constant volumetric density ρ_0, the random fissures must be distributed according to a non-uniform radial PDF $f_R(r)$, increasing radially as shown just above.
- Conversely, to obtain a non-homogeneous volumetric density, radially decreasing ($\rho(r)\downarrow$), one must specify a radial PDF $f_R(r)$ *that grows with 'r' slower than linearly.*

below summarizes more precisely the results that were obtained for some specific cases, and in particular, the case selected for the inhomogenously fissured EDZ in this paper.

Appendix B. Statistical parameters and algorithms for the generation of the radially inhomogeneous random set of 10,000 planar disc fissures in 3D

B.1. Random generation of radial positions of fissure centers. First, the random radial positions of fissures centers are generated by the following algorithm (see Table B.1).

As explained in the previous Appendix A, this leads to a decreasing radial PDF and also to a decreasing volumetric density ρ as a function of the distance from the drift wall. The relation between the PDF of radial positions and the density ρ is also explained in Appendix A.

B.2. Random generation of fissure sizes (radii). Secondly, we have parametrized the distribution of the *radii R* of planar disc fissures in such a way that '*R*' decreases significantly with distance away from the drift wall, on average (see Table B.2).

B.3. Random generation of fissure apertures. Finally, we have parametrized the statistical distribution of fissure apertures '*a*', in such a way that the aperture decreases significantly with distance away from the drift wall (see Table B.3).

Appendix C. Theoretical properties and validity of the flux superposition approach

The objective of this appendix is to present a brief discussion about the theoretical nature, the properties, and the range of validity of the "flux superposition" approach used in this work (also dubbed "frozen gradient" approach).

First, it should be made clear that the flux superposition method usually leads to an overestimation of the equivalent permeability K_{ij}. However in some cases, it is known to coïncide with the exact equivalent permeability. Here are two examples, both without matrix permeability: (i) set of parallel fractures; (ii) cartesian network of infinite size fractures considered over an infinite domain under appropriate "far field" boundary conditions.

Let us now examine more precisely the theoretical nature and validity of the flux superposition method.

- Let the symbol "ΣQ" be used for "superposition" of fluxes under a condition of frozen gradient (this is the upscaling method used in this paper);
- Let "ΣG" be used for what we call the dual method ("dual" in the sense of Fadili and Ababou, 2004), where hydraulic gradients are summed while the global flux is frozen (this superposition is "dual" with respect to the version used in this paper).

Table A.1
Volumetric density $\rho(r)$ and radial PDF of fissure centers positions $f(r)$'.

	$\rho(r)$ (volumetric density)	$f_R(r)$ (radial PDF)
Homogenous density (Poissonian positions in 3D)	$\rho(r) = \rho_0$ (constant)	$f_R(r) \propto r$
$1/r$ density(constant radial PDF)	$\rho(r) \propto 1/r$	$f_R(r) = f_0$
$1/r^{3/2}$ density[a] ($1/r$ radial PDF)[a]	$\rho(r) \propto 1/r^{3/2}$[a]	$f_R(r) \propto 1/\sqrt{r}$[a]

[a] The last case (last line of this table) corresponds to the chosen properties for the set of 10,000 fissures in the present work.

Table B.1
Random generation of radial positions of the centers of planar disc fissures: $r^{(i)} = R_{TUNNEL} + (R_{EDZ} - R_{TUNNEL}) \times (U^{(i)})^2$.

Inputs from Matlab script	*Rt* = R_{TUNNEL} = radius of 'tunnel' or drift = 2 m
`Rt = 2; widthEDZ = 4;`	*width*(*EDZ*) = EDZ annular thickness = $R_{EDZ} - R_{TUNNEL}$ = 4 m
`Afc = 2 * PI * rand;`	*rand* = "*U*" = real random number, uniformly distributed in [0, 1]
`Lfc = -Xdom/2 + Xdom * rand;`	*Alfa* = angular position of fissure centers (in a plane transverse to the 'tunnel' or drift)
`Rfc = Rt + (widthEDZ) * (rand^2);`	*Lfc* = random position of fissures centers along the drift (in the direction parallel to *X*, the axis of the drift)
	Rfc = radial position of the random centers of fissures

Table B.2
Random generation of the radii of planar disc fissures: $R^{(i)} = R_{MAX} \times \left(\frac{R_{TUNNEL}}{r^{(i)}}\right)^2$.

`Inputs from Matlab script`	Rf = $R^{(i)}$ = random radius of planar disc fissures
`Rf = FractSizeParam(1)*(Rt/Rfc)^2;`	Rfc = $r^{(i)}$ = radial position of fissure center
	R_{max} = maximal radius of fissure
Here, the specific choice for R_{max} is:	R_{MAX} = 0.40 m radius (the maximum diameter is 80 cm, at the drift wall).

Table B.3
Random generation of apertures of planar disc fissures: $a^{(i)} = a_{MAX} \times \left(\frac{R_{TUNNEL}}{r^{(i)}}\right)^2$.

Inputs from Matlab script	*aper* = $a^{(i)}$ = random aperture
`aper = aperval(family,pointer)*(Rt/Rfc)^2`	*Rfc* = $r^{(i)}$ = radial position of fissure center
	aperval = a_{MAX} = max aperture (at the drift wall)
Here, the specific choice for a_{max} is	a_{MAX} = 5.0 E − 5 m = 50 μm

Then, it is conjectured that the equivalent permeability tensors are ordered as follows:

$$(\underline{\underline{K}})^{\Sigma G} \leqslant (\underline{\underline{K}})^{EXACT} \leqslant (\underline{\underline{K}})^{\Sigma Q} \tag{A19}$$

These inequalities should be understood in the same sense as positiveness for a matrix: thus $A \leqslant B$ if matrix $B-A$ is semi-definite positive, or nonnegative. (In passing, this should provide a clearer definition of the notion of "overestimation" for a tensorial permeability).

Some inequality terms similar to those of Eq. (A19) have been demonstrated by different authors for various cases depending on geometry, heterogeneity, dimensionality. For instance, Pouya and Fouché (2009) showed for 3D fracture networks that the directional permeability obtained under boundary conditions of linearly distributed pressure, is always greater than the permeability obtained under fixed flux boundary conditions. This is analogous (although not identical), to the "ΣQ" and "ΣG" superposition methods, respectively.

However, it is not the purpose of this paper to develop further the theoretical underpinnings of inequality (Eq. (A19)), which can be viewed here, rather, as a robust conjecture. Suffice it to stress here why, and in what manner, the "ΣQ" method overestimates the true equivalent K_{ij}.

First, the type of permeability averaging implied by the present ("ΣQ") method is analogous to a weighted arithmetic mean, which tends to favor the more conducting objects over the less conducting ones. Secondly, all fractures are counted regardless of fracture connectivity (percolation effects), and this also leads to overestimating K_{ij} if the network is not fully percolating. Indeed, empirical results on synthetic 2D fracture networks with impervious matrix seem to confirm the idea that K("ΣQ") is an upper bound for the equivalent permeability tensor (Oda and Hatsuyama, 1985; Oda, 1986; Ababou et al., 1994b).

For the same reasons, the permeability obtained by the present "ΣQ" approach is quite directly related to fracture density (in fact, it is proportional to density if the matrix is impervious and all fractures have same aperture and length). But in the same case, the true equivalent permeability will not necessarily be proportional to fracture density, depending on connectivity (see for instance Bogdanov et al., 2003).

However, to temper this, one should also note that the discrepancy between K(exact) and $K(\Sigma Q)$ becomes less important as matrix permeability K_M increases. In the sequential upscaling procedure advocated in this paper, the 'matrix' is initially defined as the poorly permeable intact rock, but at the second stage, the 'matrix' represents the equivalent fissured continuum (a medium that is much more permeable than the original intact rock).

Finally, in the context of this paper (radioactive waste isolation), the important thing is that the equivalent permeability tensor K_{ij} obtained by the flux superposition method "ΣQ" is never underestimated. Thus, it is a "conservative" estimate from the point of view of waste isolation.

References

Ababou, R., 2008. Quantitative stochastic hydrogeology: the heterogeneous environment. In: Darnault, C.J.G. (Ed.), Part III of "Overexploitation & Contamination of Shared Groundwater Resources: Management, (Bio)Techno. & Political Approaches to Avoid Conflicts". NATO-ASI: Advanced Studies Institute Series, Springer Science & Business Media BV, January 2008, pp. 119–182 (Chapter. 8).

Ababou, R., Millard, A., Treille, E., Durin, M., Plas, F., 1994a. Continuum modeling of coupled thermo-hydro-mechanical processes in fractured rock. In: Peters, A. et al. (Eds.), Computational Methods in Water Resources, vol. 1. Kluwer Acad. Publishers, pp. 651–658 (Chapter 6).

Ababou, R., Millard, A., Treille, E., Durin, M., 1994b. Coupled Thermo-Hydro-Mechanical Modeling for the Near Field Benchmark Test 3 (BMT3) of DECOVALEX Phase 2: Progress Report. Rapport DMT/93/488, Commissariat à l'Energie Atomique, Saclay, France, May 1994, 202 pp.

Ababou, R., 1991. Approaches to Large Scale Unsaturated Flow in Heterogeneous, Stratified, and Fractured Geologic Media. Report NUREG/CR-5743, US Nuclear Regul. Commission, Gov. Printing Office, Washington DC, 150 pp. US.DOE web site. <http://www.osti.gov/bridge/servlets/purl/138205-ggEESe/webviewable/138205.pdf>.

ANDRA, 2005. Évaluation de la faisabilité du stockage géologique en formation argileuse. Dossier 2005 Argile. Synthèse: évaluation de la faisabilité du stockage géologique en formation argileuse. ANDRA - Agence Nationale de gestion de Déchets RadioActifs, 239pp.

Armand, G., Andra, 2007. Analyse des perméabilités mesurées autour des ouvrages du LSMHM au niveau −490 m pour déterminer des lois empiriques utilisables dans des calculs hydromécaniques couplés en milieu continu (Laboratoire de Recherche Souterrain de Meuse/Haute-Marne). Note Technique ANDRA D.NT.ALS.07.0453 A, 24 Mai 2007, 27pp.

Bailly, D., Ababou, R., Quintard, M., 2009. Geometric characterization, hydraulic behavior and upscaling of fissured geologic media. Journal of Mathematics and

Computers in Simulation, Special Issue MAMERN 2007, 79, 3385–3396. Elsevier B.V. (©2009 IMACS) doi:10.1016/j.matcom.2009.05.013.
Bogdanov, I.I., Mourzenko, V.V., Thovert, J.-F., Adler, P.M., 2003. Effective permeability of fractured porous media in steady state flow. Water Resour. Res. 39 (1), 1023. doi:10.1029/2001WR000756.
Cañamón, I., 2006. Analysis and Modeling of Coupled Thermo-Hydro-Mechanical Phenomena in 3D Fractured Media. Ph.D. Thesis (in English). Institut National Polytechnique de Toulouse (Institut de Mécanique des Fluides de Toulouse) & Universidad Politécnica de Madrid (Escuela Técnica Sup. de Ingenieros de Minas), 2006.
Cañamón, I., Elorza, F.J., Ababou, R., 2007. Thermo-Hydro-Mechanical Simulation of a 3D Fractured Porous Rock: Preliminary Study of Coupled Matrix-Fracture Hydraulics. EUROTHERM Seminar 81: Reactive Heat Transfer in Porous Media. Ecole des Mines d'Albi, France, 4–6 June 2007. Eurotherm Paper ET81-11, 8pp.
Fadili, A., Ababou, R., 2004. Dual homogenisation of immiscible steady two-phase flow in random porous media. Water Resour. Res. 40, W01513. doi:10.1029/2003WR002465.
Kiraly, L., 1969. Anisotropie et hétérogénéité de la perméabilité dans les calcaires fissurés. Eclogae Geol. Helv. (62/2), 613–619.
Oda, M., Hatsuyama, Y., 1985. Permeability tensor for jointed rock masses. In: Proceedings Internat. Symp. on Fundamentals of Rock Joints, Bjorkliden, 15–20 September 1985, pp. 303–312.
Oda, M., 1986. An equivalent continuum model for coupled stress and fluid flow analysis in fractured rock masses. Water Resour. Res. 22 (13), 1845–1856.
Papoulis, A., Pillai, S.U., 2002. Probability, Random Variables, and Stochastic Processes. Tata-McGrawHill, 852pp.
Pouya, A., Fouché, O., 2009. Permeability of 3D discontinuity networks: new tensors from boundary-conditioned homogenization. Adv. Water Resour. 32, 303–314.
Renard, P., de Marsily, G., 1997. Calculating equivalent permeability: a review. Adv. Water Resour. 20 (5–6), 253278.
Renard, P., 1997. Modélisation des écoulements en milieux poreux hétérogènes: calcul des perméabilités équivalentes. Ph.D. Thesis, Ecole Nationale Supérieure des Mines de Paris (ENSMP), Mém. Sc. de la Terre, No. 32.
Snow, D.T., 1969. Anisotropic Permeability of Fractured Media. Water Resour. Res. 5 (6), 1273–1289.
Stietel, A., Millard, A., Treille, E., Vuillod, E., Thoraval, A., Ababou, R., 1996. Continuum representation of coupled hydro-mechanical processes of fractured media: homogenisation and parameter identification. In: Stephansson, O., Jing, L., Tsang, C.-F. (Eds.), Developments in Geotech. Engg.: Coupled Thermo-Hydro-Mechanical Processes (Decovalex project for radioactive waste repositories). Developments in Geotech. Engg., 79, 135–164, Elsevier.